Published in Geochimica et Cosmochimica Acta 72, issue 22, 5475-5504, 2008
which should be used for any reference to this work

The Lithium, Boron and Beryllium content of serpentinized peridotites from ODP Leg 209 (Sites 1272A and 1274A): Implications for lithium and boron budgets of oceanic lithosphere

Flurin Vils [a,*], Laure Pelletier [a], Angelika Kalt [a], Othmar Müntener [b], Thomas Ludwig [c]

[a] *Institut de Géologie et d'Hydrogéologie, Université de Neuchâtel, Rue Emile-Argand 11, CP 158, CH-2009 Neuchâtel, Switzerland*
[b] *Institut de Minéralogie et Géochimie, Université de Lausanne, Anthropole, CH-1015 Lausanne, Switzerland*
[c] *Mineralogisches Institut, Ruprecht-Karls-Universität Heidelberg, Im Neuenheimer Feld 236, D-69120 Heidelberg, Germany*

Abstract

Despite the key importance of altered oceanic mantle as a repository and carrier of light elements (B, Li, and Be) to depth, its inventory of these elements has hardly been explored and quantified. In order to constrain the systematics and budget of these elements we have studied samples of highly serpentinized (>50%) spinel harzburgite drilled at the Mid-Atlantic Ridge (Fifteen–Twenty Fracture zone, ODP Leg 209, Sites 1272A and 1274A). In-situ analysis by secondary ion mass spectrometry reveals that the B, Li and Be contents of mantle minerals (olivine, orthopyroxene, and clinopyroxene) remain unchanged during serpentinization. B and Li abundances largely correspond to those of unaltered mantle minerals whereas Be is close to the detection limit. The Li contents of clinopyroxene are slightly higher (0.44–2.8 $\mu g\ g^{-1}$) compared to unaltered mantle clinopyroxene, and olivine and clinopyroxene show an inverse Li partitioning compared to literature data. These findings along with textural observations and major element composition obtained from microprobe analysis suggest reaction of the peridotites with a mafic silicate melt before serpentinization. Serpentine minerals are enriched in B (most values between 10 and 100 $\mu g\ g^{-1}$), depleted in Li (most values below 1 $\mu g\ g^{-1}$) compared to the primary phases, with considerable variation within and between samples. Be is at the detection limit. Analysis of whole rock samples by prompt gamma activation shows that serpentinization tends to increase B (10.4–65.0 $\mu g\ g^{-1}$), H_2O and Cl contents and to lower Li contents (0.07–3.37 $\mu g\ g^{-1}$) of peridotites, implying that—contrary to alteration of oceanic crust—B is fractionated from Li and that the B and Li inventory should depend essentially on rock–water ratios. Based on our results and on literature data, we calculate the inventory of B and Li contained in the oceanic lithosphere, and its partitioning between crust and mantle as a function of plate characteristics. We model four cases, an ODP Leg 209-type lithosphere with almost no igneous crust, and a Semail-type lithosphere with a thick igneous crust, both at 1 and 75 Ma, respectively. The results show that the Li contents of the oceanic lithosphere are highly variable (17–307 kg in a column of 1 m × 1 m × thickness of the lithosphere (kg/col)). They are controlled by the primary mantle phases and by altered crust, whereas the B contents (25–904 kg/col) depend entirely on serpentinization. In all cases, large quantities of B reside in the uppermost part of the plate and could hence be easily liberated during slab dehydration. The most prominent input of Li into subduction zones is to be expected from Semail-type lithosphere because most of the Li is stored at shallow levels in the plate. Subducting an ODP Leg 209-type lithosphere would mean only very little Li contribution from the slab. Serpentinized mantle thus plays an important role in B recycling in subduction zones, but it is of lesser importance for Li.

1. INTRODUCTION

At mid-ocean ridges, plates spread and new oceanic lithosphere is produced. At slow spreading-ridges, the

* Corresponding author. Fax: +41 32 718 26 01.
E-mail address: flurin.vils@unine.ch (F. Vils).

magmatic section is often reduced and the oceanic mantle is exhumed at the ocean floor (e.g. Cannat, 1993; Michael et al., 2003; Escartin et al., 2003). The two currently debated models to explain mantle exhumation in slow-spreading environments invoke either spreading, and focused magmatism at the center of a ridge segment (Cannat, 1993; Ghose et al., 1996 and Dijkstra et al., 2001) or detachment faulting (Tucholke et al., 1998; Escartin et al., 2003; Boschi et al., 2006; Ildefonse et al., 2007). In both cases, hydrothermal fluids transform olivine, orthopyroxene and clinopyroxene into serpentine, chlorite, tremolite, brucite or magnetite (e.g. Bach et al., 2004), depending on temperature and pressure conditions (e.g. Ulmer and Trommsdorff, 1995).

In the last years, the systematics of the light elements Li, B, and Be have been used to chemically trace low-temperature alteration processes in different geological environments (e.g. James and Palmer, 2000; Chan et al., 2002; Pistiner and Henderson, 2003; Rudnick et al., 2004; Kisakürek et al., 2004). Studies on fresh mid-ocean ridge basalts (MORB; Ryan and Langmuir, 1987; Ryan and Langmuir, 1993) and on altered MORB (e.g. Thompson and Melson, 1970; Bouman et al., 2004; Elliott et al., 2006) showed that during alteration Li and B may be enriched by a factor of 2 and 30, respectively.

A similar reasoning can be applied to the underlying mantle lithosphere. Estimates of the light element content of the primitive mantle (McDonough and Sun, 1995; Lyubetskaya and Korenaga, 2007) and of the depleted mantle (Salters and Stracke, 2004) imply very low light element abundances in whole rock samples and major mantle phases (around 1 $\mu g\,g^{-1}$ for Li and B). These whole rock data are consistent with C1 chondrite concentrations (Anders and Grevesse, 1989; Lyubetskaya and Korenaga, 2007). In contrast, elevated Li (up to 13.7 $\mu g\,g^{-1}$, Decitre et al., 2002; Niu, 2004) and high B whole rock contents (up to 85 $\mu g\,g^{-1}$, Bonatti et al., 1984; Spivack and Edmond, 1987) were found in dredged abyssal peridotites. High Li (<19.5 $\mu g\,g^{-1}$, Decitre et al., 2002) and B abundances (~47 $\mu g\,g^{-1}$, Scambelluri et al., 2004) were found in serpentine minerals.

In addition, high but variable whole rock B (0.4–79.0 $\mu g\,g^{-1}$; Benton et al., 2001; Savov et al., 2005; Wei et al., 2005) and Li concentrations (0.5–18.9 $\mu g\,g^{-1}$; Parkinson and Pearce, 1998; Benton et al., 2004; Savov et al., 2005; Zanetti et al., 2006; Savov et al., 2007) were measured in serpentinized peridotites from forearc settings.

Beryllium (Be) data are scarce, and concentrations are extremely low in primitive mantle (0.054 $\mu g\,g^{-1}$ or 0.068 $\mu g\,g^{-1}$; McDonough and Sun, 1995; Lyubetskaya and Korenaga, 2007) and in depleted mantle (0.025 $\mu g\,g^{-1}$; Salters and Stracke, 2004), highly variable in dredged abyssal peridotites (0.001–0.212 $\mu g\,g^{-1}$, Niu, 2004), and elevated in forearc peridotites (0.07–0.16 $\mu g\,g^{-1}$, Zanetti et al., 2006).

Experimentally determined mineral/melt and mineral/fluid partition coefficients are in line with these observations and show that B, Li and Be are incompatible in mantle minerals (e.g. Brenan et al., 1998; Taura et al., 1998). However, there are only a few experiments concerning the light element contents of hydrothermally precipitated minerals. Seyfried and Dibble (1980) performed seawater–peridotite experiments at 300 °C and 500 bar. During the experiment, the B content in the solution (pH <5) remained constant, but during quenching the B content decreased from 4.01 to 1.75 $\mu g\,g^{-1}$. It was proposed that B is incorporated into serpentinized peridotite at low temperatures (<300 °C). Bonatti et al. (1984) suggested that the maximum B uptake in peridotite is related to temperature and to the serpentine polymorph, and measured a maximum value of 110 $\mu g\,g^{-1}$ B in serpentine minerals (orthochrysotile, clinochrysotile and lizardite). Reversing the alteration process by heating up altered basalt to 350 °C at 500 bar showed that Li and B are incorporated in low-temperature alteration phases and are liberated into the fluid phase upon heating (Seyfried et al., 1998).

The light element content of the oceanic mantle is important in the context of recycling of these elements in subduction zones. Previous studies have shown that the magmatic and sedimentary oceanic crust can be a major host for Li and B. Oceanic sediments are enriched in B (up to 100.2 $\mu g\,g^{-1}$, Leeman et al., 2004) and Li (up to 74.3 $\mu g\,g^{-1}$, Bouman et al., 2004; Leeman et al., 2004). Even after metamorphism at high pressure and moderate temperature (~400 °C) in a subduction zone, they retain up to 66.7 $\mu g\,g^{-1}$ Li, 2.32 $\mu g\,g^{-1}$ Be, and 93.9 $\mu g\,g^{-1}$ B (Marschall et al., 2006). Altered oceanic basalt may contain up to 36.5 $\mu g\,g^{-1}$ Li (Bouman et al., 2004). Subducted oceanic crust, nowadays eclogites, was found to contain up to 37.4 $\mu g\,g^{-1}$ Li (Zack et al., 2002; Marschall et al., 2006), and up to 4.77 $\mu g\,g^{-1}$ B (Marschall et al., 2006). However, the crustal section of a subducting oceanic lithosphere is thin compared to the mantle part and magmatic crust can be largely absent in lithosphere produced at slow-spreading ridges. Therefore, serpentinized mantle should play a key role in light element recycling. Experiments on serpentinite breakdown (simulation of a subducting plate) by Tenthorey and Hermann (2004) suggest that serpentinized mantle should be the major sink of B in subduction zones. The extreme enrichment in B of the Mariana forearc mantle wedge supports this theory (Savov et al., 2007).

In this study, we investigated serpentinized oceanic peridotite drilled from near the Mid-Atlantic Ridge (MAR, ODP Leg 209, Sites 1272A and 1274A). We analyzed minerals and whole rock samples for major elements, Li, Be and B contents. Our aims were to identify the host minerals of the light elements, to understand light element systematics, to establish a mass balance and to discuss the calculations in the framework of light element recycling at subduction zones.

2. GEOLOGICAL SETTING

ODP Leg 209 was drilled at the MAR, north and south of the Fifteen–Twenty Fracture zone (Fig. 1, Kelemen et al., 2004a; Paulick et al., 2006; Kelemen et al., 2007). A full spreading rate of 25 mm/year was determined (Fujiwara et al., 2003), corresponding to a slow-spreading ridge. The half-spreading rates (E and W) show little long-term

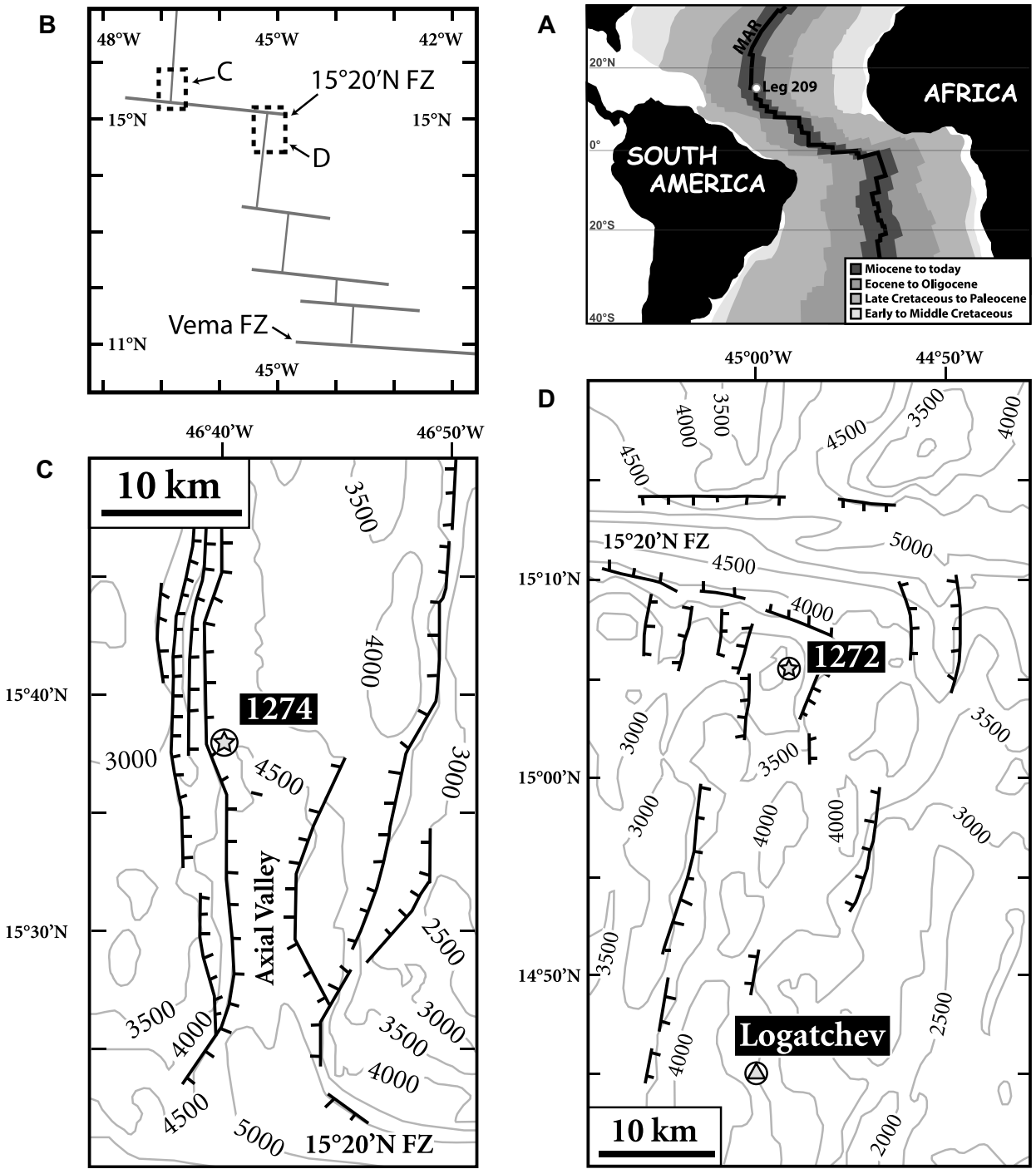

Fig. 1. (A) Isochrone map illustrating the age of the Atlantic ocean (modified after Scotese et al., 1988) and displaying ODP Leg 209 on the Mid-Atlantic Ridge (MAR). (B) Details of drill sites of the Northern and the Southern areas of ODP Leg 209. (C and D) Bathymetric map (after Lagabrielle et al., 1998) showing the location of ODP Sites 1272A and 1274A (stars; modified after Paulick et al., 2006). The Logachev active hydrothermal field is also shown (triangle).

asymmetry. This inspired Fujiwara et al. (2003) and later Escartin et al. (2003) to propose a model of shallow detachment faults to explain the geomorphologic and geologic situation around the Fifteen–Twenty Fracture zone. The major difference with respect to previously proposed models (amagmatic extension or melt-assisted extension; e.g. Tucholke et al., 1998; Dick et al., 2003) is the rooting of detachment faults in the shallow lithosphere, probably coinciding with the rheological boundary between the alteration (serpentinization) front and the unaltered litho-

sphere. Mostly ultrabasic rocks crop out in this area, covered by a thin sediment layer (Kelemen et al., 2004a; Kelemen et al., 2007).

The mineralogical composition and evolution of the peridotites at the two drilling sites (1272A and 1274A) is considered to be different (Seyler et al., 2007; Godard et al., 2008). Site 1272A has less abundant clinopyroxene than Site 1274A and seems to reflect partial melting and melt extraction, while Site 1274A records in addition pervasive melt–rock interaction (Seyler et al., 2007; Godard et al., 2008).

35 miles south of the Fifteen–Twenty Fracture zone (44°58′N 14°45′W, Sudarikov and Roumiantsev, 2000), the Logatchev hydrothermal field is located on the rift flank. It was discovered during several Russian expeditions in the 90s. It is situated within steeply faulted blocks of ultramafic rocks, which experienced variable degrees of serpentinization (Sharapov and Simonov, 1991). Basalts and gabbros are commonly exposed around the vent sites (Escartin and Cannat, 1999; Kuhn et al., 2004; Schmidt et al., 2007). Recent expeditions studied the hydrothermal fluids in more detail. The latter contain 1.75 $\mu g\,g^{-1}$ Li and 3.63 $\mu g\,g^{-1}$ B at a temperature of 353 °C and a pH of 3.3 (Douville et al., 2002; Schmidt et al., 2007).

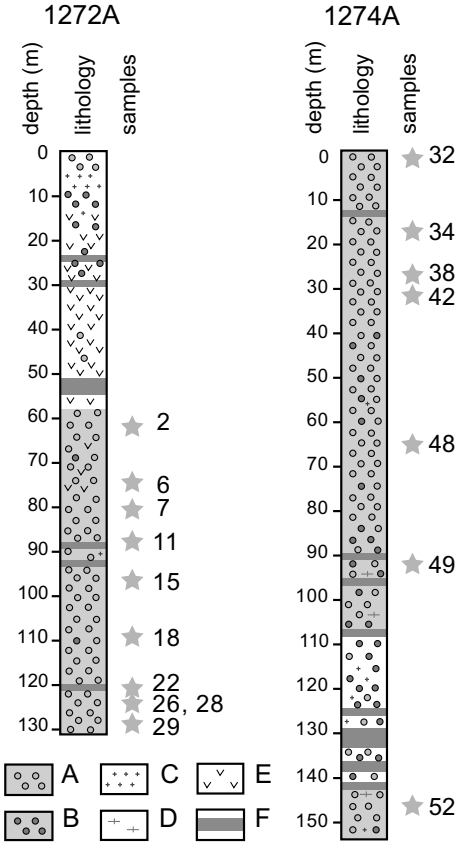

Fig. 2. Core description and sample location for ODP Leg 209, modified after Bach et al. (2004). (A) Harzburgite, (B) dunite, (C) gabbro, (D) magmatic dikelets, (E) basalt and diabase, (F) fracture zone. Numbers correspond to sample numbers (e.g. 26 = OD 26).

3. SITE AND SAMPLE CHARACTERISTICS

3.1. Site 1272A

Site 1272A was drilled at a water depth of 2560 m at the ridge (Fig. 1). The drilled material consists of ~55 m diabase in the upper part, and 75 m of harzburgite containing rare dunite in the lower part (Fig. 2; Kelemen et al., 2004a). The major mineral phase in the mantle rocks is lizardite, and a downhole decrease in serpentinization can be observed (Kelemen et al., 2004a). Modal mineralogy and petrographic features of the analyzed spinel harzburgites are summarized in Table 1 and Fig. 2.

The studied samples were collected from the lower part of the drill core, at depths between 61.75 and 129.42 m.b.s.f. (meters below sea floor) and are serpentinized spinel harzburgites (Fig. 2). Macroscopically, the samples have a dark green to whitish green color. Some white veins can be observed and a dark vein occurs in sample OD 11. In most samples, porphyroclastic orthopyroxene forms large (<1 cm) grains, which are surrounded by dark green serpentine. They are distributed irregularly in a homogeneous matrix of serpentine minerals.

The degree of serpentinization ranges from 70% to 99% and tends to decrease with increasing depth. Apart from serpentine minerals and orthopyroxene, the samples may contain variable proportions of olivine, clinopyroxene, spinel and magnetite (Table 1). Olivine, pyroxenes and spinel are 'primary' minerals related to mantle processes, while serpentine and magnetite are of secondary origin, related to serpentinization. Olivine forms isolated, large fragments within serpentine (Fig. 3c). Orthopyroxene grains may show exsolution lamellae of clinopyroxene (Fig. 3b). Clinopyroxene occurs as interstitial phase at orthopyroxene grain boundaries (Fig. 3a). Magnetite forms euhedral grains and symplectites with spinel (Fig. 3d).

The terminology of Wicks and Whittaker (1977) is used to describe the serpentine textures of the studied samples. We observe pseudomorphic textures after olivine and orthopyroxene, vein textures, as well as non-pseudomorphic textures. Bastite after orthopyroxene (in the following termed bastite; Fig. 3a) is the most common type of pseudomorphic serpentine texture in the studies rocks. Often, pseudomorphs of clinopyroxene exsolution lamellae are preserved within bastite, as described by Viti et al. (2005). Serpentine pseudomorphing olivine in mesh and hourglass textures (O'Hanley, 1996) is also abundant (Fig. 3c). The inner parts of mesh rims are often reddish brown to black. In bastite, the reddish-brown colors are attributed to the presence of brucite (Wicks and Whittaker, 1977). All samples display picrolite vein textures (lizardite according to Bach et al., 2004) and chrysotile asbestos cross-fiber veins (Fig. 3e, f). While chrysotile veins crosscut bastites and are distributed randomly within the samples, lizardite picrolites are preferably found along mineral boundaries and natural weak zones (e.g. OD 28). Iowaite, as described by Bach et al. (2004), and brucite could not be identified directly using SEM or EMP. We found some magnetite strings (Fig. 3e) in samples OD 2, OD 22 and OD 29.

Table 1
ODP sample names and modes

Working no.	Sample depth [m.b.s.f.]	ODP sample no.	Modes (%)					Modes serp min. (%)			
			Cpx	Opx	Ol	Spl	Serp	Ba	Pi	Cy	Aom
Leg 1272A											
OD 2	61.75	209-1272A-13R-1, 103.5-106.5	0	0	3	3	94	30	–	2	62
OD 6	76.53	209-1272A-16R-2, 6-8	0	0	1	2	97	40	7	3	47
OD 7	80.18	209-1272A-17R-1, 57-60	0	0	0	4	96	40	3	1	52
OD 11	89.92	209-1272A-19R-1, 60-64	0	0	0	1	99	55	4	2	38
OD 15	99.85	209-1272A-21R-1, 102-108	0	0	0	3	97	30	2	2	63
OD 18	110.19	209-1272A-23R-2, 22-25	0	0	0	1	99	39	2	2	56
OD 22	120.05	209-1272A-25R-2, 67-71	0	0	0	2	98	32	1	2	63
OD 26	125.08	209-1272A-26R-2, 66-72	0	18	10	2	70	40	–	5	25
OD 28	127.30	209-1272A-27R-1, 28-31.5	1	15	10	1	73	25	2	4	42
OD 29	129.42	209-1272A-27R-2, 90-95	0.5	10	18	1.5	70	30	2	1	37
Leg 1274A											
OD 32	0.89	209-1274A-1R-1, 88-92	3	27	13	5	52	35	–	2	15
OD 34	17.27	209-1274A-3R-1, 35-38	1	23	15	2	59	25	–	4	30
OD 38	27.54	209-1274A-5R-1, 123-125	1	25	14	2	58	30	–	3	25
OD 42	32.14	209-1274A-6R-2, 68-70	1	10	15	2	72	20	17	5	30
OD 48	69.79	209-1274A-14R-1, 76-82	1	30	15	3	51	25	–	3	23
OD 49	94.11	209-1274A-18R-1, 80-83	0	0	0	3	97	20	–	10	67
OD 52	146.69	209-1274A-27R-1, 56-61	1	15	15	5	64	26	–	3	35

Cpx, clinopyroxene; opx, orthopyroxene; ol, olivine; spl, spinel; serp, serpentine; ba, bastite; pi, picrolite; cy, chrysotile; and aom, after ol and matrix.

3.2. Site 1274A

The drill hole is located on the western flank of a seamount at a water depth of 3940 m, in a weathered area north of the Fifteen–Twenty fracture zone (Fig. 1). Beneath 2 m of sediment, a total of 155.8 m of mantle rocks was drilled (Fig. 2). The site was divided into 3 units (Kelemen et al., 2004a). Unit I (top) and III (bottom) are serpentinized harzburgites, whereas unit II (middle) is interpreted as a 50-m fault gouge (mostly peridotite clasts within a mud matrix, all brecciated; Kelemen et al., 2004a).

The studied samples are from unit I, except OD 52 (unit III). They are all serpentinized spinel harzburgites. In unit I, serpentinization increases from the top to the base (Table 1). Macroscopically, the samples are all dark green with orthopyroxene blasts of up to 1 cm size. Rarely, whitish veins can be found. Samples OD 34 and OD 42 are crosscut by a large serpentine vein (up to 0.4 cm wide). The brownish color of some veins under the optical microscope could be related to brucite (Wicks and Whittaker, 1977).

The primary phases are olivine, orthopyroxene and clinopyroxene, all with the same textural characteristics as at Site 1272A. In addition, one large grain of primary clinopyroxene with exsolution lamellae of (serpentinized) orthopyroxene is preserved (sample OD 32, Fig. 3b). Also, sample OD 42 contains a cluster of small olivine grains (Fig. 3f) associated with chlorite and phlogopite. This assemblage most likely represents a micro-gabbroic pocket and is probably related to the magmatic vein crosscutting the drillcore between 31.95 and 32.45 m.b.s.f. (Kelemen et al., 2004b, core description). Such small gabbroic pockets were also identified in the MARK area (Niida, 1997). In the following, this olivine will be termed 'magmatic'. Spinel forms symplectites with clinopyroxene (Fig. 3d), growing into orthopyroxene. This process preferably starts at boundaries between orthopyroxene grains and between orthopyroxene and olivine.

Serpentine mineral textures and vein types correspond to those described for Site 1272A. Magnetite is more abundant in the picrolite veins than within mesh structures. In bastite, relicts of orthopyroxene show serrate boundaries indicating ongoing serpentinization (Wicks and Whittaker, 1977). In OD 48 and OD 49, magnetite forms thick ribbons (Fig. 3f), crosscutting through the entire thin section. They are interpreted as ancient picrolite veins. Sample OD 34 contains Ni-bearing sulfides. Rare iowaite ($Mg_4(OH)_8FeOCl_2 \cdot nH_2O$ [$n = 1$–4]) could be identified in sample OD 34, but was too small to be quantitatively analyzed.

The size of mineral grains in both sites is 50–500 μm for olivine, 50–1000 μm for orthopyroxene and 30–80 μm for clinopyroxene. Serpentine mineral grain size is much lower than the resolution of SEM, except for chrysotile veins (Fig. 3e), where asbestos fibers are visible at SEM scale. They probably form late-stage fracture filling (Prichard, 1979).

4. ANALYTICAL TECHNIQUES

The major element compositions of olivine, clinopyroxene, orthopyroxene, spinel, magnetite and serpentine minerals were determined by electron microprobe analysis (EPMA) using a JEOL JXA-8200 (University of Bern, and ETH Zürich, Switzerland), a Cameca SX-51 (University of Heidelberg, Germany) and a SX-100 (University of Freiburg, Germany), all equipped with wavelength-dispersive systems. An accelerating potential of 15 kV, a beam current of 20 nA and counting times of 30 s for Si, Al, Mg and Na and 20 s for the other elements were used. Minerals and synthetic glasses were used as standards. Samples were analyzed with a spot

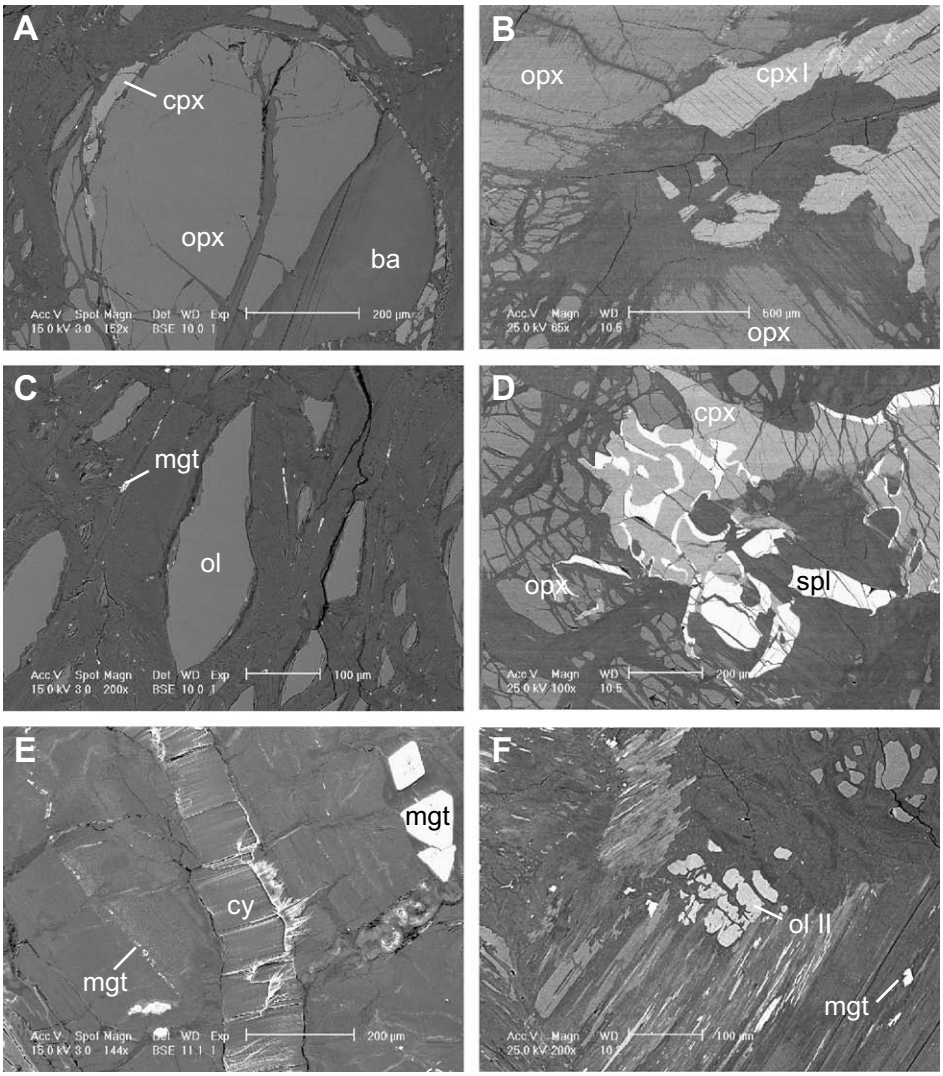

Fig. 3. Backscattered images of the different mineral phases from the ODP Sites 1272A (A, C, and D) and 1274A (B, D, and F); scale bars on the image. (A) Primary orthopyroxene with interstitial clinopyroxene (cpx) and bastite after opx (sample OD 29). (B) Primary clinopyroxene with exsolution lamellae of opx, now serpentinized (sample OD 32). (C) Relicts of primary olivine surrounded by serpentine in mesh textures. Magnetite can be found in small picolite veins (sample OD 29). (D) Spinel (spl) with clinopyroxene (cpx) overgrowing orthopyroxene (sample OD 32). (E) Chrysotile vein (cy) in a completely serpentinized harzburgite (sample OD 2). (F) Cluster of magmatic olivine (ol II) in a serpentine matrix (sample OD 42).

size of approximately 1 μm. For serpentine minerals, analyses with a 1 μm and a 15 μm spot size provided identical results within the analytical error of the microprobe (Table 2). Therefore, a 1 μm spot size was chosen to obtain a better spatial resolution.

Li, B and Be were analyzed in-situ on polished thin sections by Secondary Ion Mass Spectrometry (SIMS) using a modified Cameca IMS 3f ion microprobe at the Mineralogical Institute of Heidelberg, Germany. A 14.5 keV/20 nA $^{16}O^-$ primary beam with ~30 μm diameter and acceleration to a nominal energy of 4.5 keV for the positive secondary ions was used. Secondary ^{7}Li, ^{9}Be, ^{11}B and ^{30}Si ions were collected applying the energy filtering method using an offset of 75 eV at a mass resolution of ~1030 ($m/\Delta m$, 10%) and a nominal imaged field of 25 mm. Secondary ion intensities were normalized to the count rates of ^{30}Si and calibrated against the NIST SRM610 glass reference material using the concentrations (preferred averages) reported in Pearce et al. (1997); the accuracy is estimated to be <20% for Li and <10% for Be and B (Ottolini et al., 1993). Li, B and Be concentrations were quantified using the SiO_2 values of the corresponding EPMA analysis. One single analysis comprised 10 cycles for each isotope with integration times of 8 s/cycle for Li, 16 s/cycle for Be and B, and 2 s/cycle for Si. The mass spectrometer's and the counting system's background of 0.02 ions/s where determined independently ('well known background'). The setup chosen and the background lead to a detection limit (critical value) of 1.4 ng g^{-1} (Li), 1.0 ngg^{-1} (Be) and 2.6 ng g^{-1} (B) (Currie, 1968; Marschall and Ludwig, 2004).

Due to the generally low concentration levels of Li, Be and B in mantle rocks, contamination during sample preparation and handling is always problematic, particularly for B (Shaw et al., 1988). Careful sample preparation is thus a necessary prerequisite for accurate analyses. The standard protocol established by Marschall and Ludwig (2004) was used to prepare the thin sections for this study at the Mineralogical Institute of Heidelberg. Carbon-coated samples were used for BSE investigation (textures) and electron microprobe analyses (major element composition of minerals; see further on). At the beginning of each SIMS analysis,

Table 2
Results of electron microprobe analysis of serpentine with different spot size, all Fe considered as Fe^{2+}

OD32	sela	selb	se9a	se9b
SiO_2	40.51	41.49	39.26	39.37
TiO_2	0.02	0.00	0.00	0.00
Cr_2O_3	0.95	0.94	1.45	1.39
Al_2O_3	2.79	2.58	0.03	0.00
FeO	4.47	4.72	6.78	6.68
MnO	0.07	0.12	0.18	0.12
MgO	36.72	37.10	36.37	36.47
CaO	0.10	0.13	0.17	0.14
Na_2O	0.04	0.04	0.04	0.02
K_2O	0.02	0.02	0.01	0.00
H_2O	12.45	12.66	12.07	12.07
Cl	0.17	0.15	0.16	0.17
Total	98.30	99.96	96.51	96.44
F,Cl=O	0.04	0.03	0.04	0.04
Total	98.26	99.93	96.48	96.40
Cat	4.959	4.954	5.015	5.012
Spot size	1 μm	15 μm	1 μm	15 μm

Cat, total cations.

a presputtering of ~400 s was applied to eliminate the potential rest of surface contamination. Additionally, the imaged field was set smaller than the primary beam diameter (applying field aperture #2, $d = 750$ μm) to suppress contaminating secondary ions from the crater edges (Benninghoven et al., 1987). Following the procedure described by Marschall and Ludwig (2004), the B contamination level is <2 ng g^{-1}. Li contamination is typically ~50 times less than for B, and Be does not show any sign of contamination.

The area analyzed by SIMS has a diameter of ~12 μm (determined by the field aperture and the nominal imaged field), but all serpentine minerals have smaller grain size (<0.5 μm; Fig. 3). This means that one SIMS analysis corresponds to several grains of serpentine and in some cases to mixtures of serpentine and other minerals such as magnetite, brucite or small fluid inclusions. However, the fraction of non-serpentine minerals included in a SIMS analysis was small as can be depicted from the major element composition (Table 3).

Whole rock concentrations of major elements and their oxides and some trace elements (H, B, and Cl) of 14 samples were determined using the prompt gamma activation analysis (PGAA) facility at the Budapest Research Reactor (Hungary). PGAA is especially useful for analyzing whole rock boron, chlorine and hydrogen concentrations. In contrast to other geoanalytical methods, sample preparation procedures are not needed, and hence contamination problems are eliminated (Anderson and Kasztovszky, 2004). Accuracy of trace element analyses by PGAA was checked by measurements of geological reference materials (Gméling et al., 2005) and of natural samples (Marschall et al., 2005). The spectra were evaluated with Hypermet-PC software; the element identification was performed using a prompt-gamma library (Révay et al., 2001). The H_2O content of the sample is determined by stoichiometry.

Each sample (0.3–4.5 g) was hot-sealed in a fluorinated ethylene propylene (FEP) film (about 20 × 30 mm), which produces a negligible background. The analytical setup was described by Molnar (2004). All of the samples were thinner than 5 mm; thus the self-absorption of neutrons and γ-photons was negligible. The measurement time for each individual sample varied between 4500 and 10,000 s (OD 26: 55,000 s).

5. RESULTS

5.1. Major and light element contents of minerals

Concentrations of major and light elements are given in Tables 3 and 4, respectively. Primary olivine is homogeneous with an average Mg# of 0.91 ($Mg\# = 100 \times Mg/[Mg + Fe_{tot}]$, all iron assumed as divalent), and NiO contents of ~0.4 wt% (Fig. 4). Magmatic olivine in sample OD 42 (Fig. 3f) has a Mg# of 0.80 and NiO contents of 0.1–0.2 wt%. Average light element contents of primary olivine are 1.04 μg g^{-1} for Li, 0.022 μg g^{-1} for B, and below the critical value for Be. They are higher in magmatic olivine of sample OD 42 (Li 8.29 μg g^{-1}, B 0.54 μg g^{-1} and Be 9.8 ng g^{-1}). There is no core-to-rim variation in major and light elements for primary olivine; magmatic olivine is too small to detect zoning.

5.1.1. Pyroxenes

Orthopyroxene is homogeneous and not zoned, with an average Mg# of 0.91 (Table 3c). The Al_2O_3 and Cr_2O_3 contents are quite variable (1.4–2.3 wt% Al_2O_3 and 0.1–1.1 wt% Cr_2O_3) and positively correlated (Fig. 5a), with the exception of sample OD 52. Average light element contents of orthopyroxene are 0.7 μg g^{-1} Li, 0.011 μg g^{-1} B and below the critical value for Be. There is no core-to-rim variation in major and light elements for orthopyroxene (profile in Table 4, OD22C3opp1–1 to 1–6, rim to core).

Primary clinopyroxene in sample OD 32 is zoned. The rim is enriched in Mg and Si, depleted in Al and Cr compared to the core (Fig. 6). The rim composition of the primary clinopyroxene is similar to the composition of interstitial clinopyroxene (Fig. 6). The light element contents show no difference between rim and core. The average values are 1.5 μg g^{-1} for Li, 0.07 μg g^{-1} for B, and below critical value for Be. Interstitial clinopyroxene has Mg# between 0.91 and 0.95, CaO is 20–25 wt%, $Na_2O \leqslant 0.2$ wt% and $TiO_2 \leqslant 0.2$ wt%. Interstitial clinopyroxene has average light element contents of 2.05 μg g^{-1} Li, 0.89 μg g^{-1} B and 8.6 ng g^{-1} Be, higher than those of primary clinopyroxene.

5.1.2. Serpentine minerals

There is no systematic difference in the major and light element composition of serpentine minerals from different textures (see section 'Site and sample characteristics'). Serpentine minerals have SiO_2 between 39.1 and 42.0 wt% and an average FeO content of 4.3 wt%. NiO is below 0.44 wt%. Cr_2O_3 is below 0.81 wt%. Analyses within serpentine matrix give lower oxide totals than analyses of other serpentine textures, but calculated cations normalized to nine oxygens are conform with serpentine stoichiometry. The light element content of the serpentine minerals is highly variable, ranging from 0.002 to 9.37 μg g^{-1} Li, and from 0.09 to 138 μg g^{-1} B. The results of micro-Raman analyses performed on some of the spots analyzed for light element concentrations by SIMS showed that in cases where Li concentrations exceed 1 μg g^{-1}, serpentine (lizardite) is mixed with orthopyroxene (Pelletier, 2008). The average light element abundances in serpentine of our

Table 3
Representative analyses of major phases

3a																	
Mineral	Olivine (normalized to four oxygens)																
Sample	OD 2 o2c6ol3	OD 6 o6c2sp4	OD 26 o26c3ol4c	OD 28 o28c3ol2r	OD 29 o29c5ol3c	OD 38 dp38ol1	OD 32 dp32ol1	OD 32 dp32ol4	OD 34 OD34ol3	OD 34 OD34ol5	OD 42 42ol1	OD 42 42ol4	OD 48 48ol4	OD 48 48ol5	OD 52 oD52ol2	OD 52 OD52ol3	OD 52 odp52ol4
SiO_2	41.15	41.60	39.99	40.83	40.68	41.47	41.14	41.16	41.15	40.91	40.66	40.74	40.72	40.75	41.06	40.61	40.73
TiO_2	<0.01	0.01	<0.01	<0.01	0.01	<0.01	<0.01	<0.01	<0.01	0.01	<0.01	<0.01	0.01	0.02	<0.01	<0.01	<0.01
Cr_2O_3	0.07	0.02	0.01	<0.01	0.01	0.03	0.05	0.03	<0.01	0.02	<0.01	0.01	<0.01	<0.01	<0.01	<0.01	0.04
Al_2O_3	0.03	0.04	<0.01	0.01	<0.01	0.01	0.02	0.02	<0.01	0.02	0.04	<0.01	<0.01	0.02	0.02	<0.01	0.01
FeO	8.21	8.59	8.34	8.958	8.33	8.93	9.30	9.40	8.44	8.33	8.75	8.78	8.95	8.44	8.06	7.92	8.14
MnO	0.10	0.17	0.12	0.10	0.12	0.11	0.21	0.09	0.13	0.11	0.14	0.14	0.11	0.13	0.09	0.15	0.03
NiO	0.28	0.4	0.36	0.35	0.41	0.39	0.35	0.39	0.44	0.45	0.40	0.37	0.39	0.36	0.18	0.40	0.51
MgO	50.59	50.55	51.95	50.26	49.63	50.26	50.82	50.88	50.15	50.46	50.38	50.18	50.66	50.61	50.30	50.56	50.26
CaO	0.10	0.06	0.04	0.05	0.05	0.08	0.08	0.10	0.06	0.05	0.03	0.03	0.02	0.05	0.03	0.03	0.04
Total	100.54	101.49	100.83	100.57	99.28	101.29	101.97	102.06	100.37	100.36	100.45	100.26	100.87	100.37	99.73	99.68	99.76
Si	0.997	1.000	0.970	0.991	0.999	1.000	0.989	0.988	1.000	0.994	0.990	0.993	0.988	0.991	1.001	0.992	0.995
Ti	0.000	0.000	0.000	0.000	0.000	0.000	0.000	0.000	0.000	0.000	0.000	0.000	0.000	0.000	0.000	0.000	0.000
Cr	0.001	0.000	0.000	0.000	0.000	0.001	0.001	0.001	0.000	0.000	0.000	0.000	0.000	0.000	0.000	0.000	0.001
Al	0.001	0.001	0.000	0.000	0.000	0.000	0.001	0.001	0.000	0.000	0.001	0.000	0.000	0.001	0.001	0.000	0.000
Fe	0.166	0.173	0.169	0.174	0.171	0.180	0.187	0.189	0.171	0.169	0.178	0.179	0.182	0.172	0.164	0.162	0.166
Mn	0.002	0.003	0.003	0.002	0.002	0.002	0.004	0.002	0.003	0.002	0.003	0.003	0.002	0.003	0.002	0.003	0.001
Ni	0.005	0.009	0.007	0.007	0.008	0.008	0.007	0.008	0.009	0.009	0.008	0.007	0.008	0.007	0.004	0.008	0.010
Mg	1.827	1.811	1.879	1.833	1.817	1.806	1.820	1.821	1.816	1.828	1.828	1.823	1.832	1.834	1.827	1.841	1.830
Ca	0.003	0.002	0.001	0.001	0.001	0.002	0.002	0.003	0.001	0.001	0.001	0.001	0.001	0.001	0.001	0.001	0.001
Cat	3.002	2.999	3.030	3.009	3.000	3.000	3.011	3.011	3.000	3.005	3.011	3.007	3.012	3.009	2.999	3.008	3.005
Mg#	0.917	0.913	0.917	0.913	0.914	0.909	0.907	0.906	0.914	0.915	0.911	0.911	0.910	0.914	0.918	0.919	0.917

3b (*continued*)

Mineral	Clinopyroxene (normalized to 6 oxygens)																
Sample	OD 26 o26c5cp2c	OD 28 o28c2cp2c	OD 29 o29c1cp2c	OD 38 dp38cpc9	OD 32 dp32cpc1	OD 32 dp32cpc1	OD 32 dp32cpc1	OD 32 dp32cpc1	OD 32 dp32cpx2	OD 32 dp32cpx5	OD 34 odp34cpi3	OD 42 42cpr1	OD 42 42cpr3	OD 42 42cp3b	OD 48 48cp5	OD 48 48cp6	OD 52 odp52cp1
SiO_2	52.00	52.43	53.30	52.86	51.94	52.22	51.35	53.69	52.92	52.72	52.36	52.77	52.85	52.93	52.34	52.50	52.60
TiO_2	0.05	0.01	0.03	0.04	0.01	0.06	0.02	0.06	0.04	0.05	0.03	0.05	0.05	0.04	0.14	0.13	0.13
Cr_2O_3	1.32	1.21	1.04	1.16	1.58	1.55	1.61	0.57	1.18	1.24	1.45	2.92	3.28	3.21	1.40	1.13	1.57
Al_2O_3	3.11	2.77	2.65	3.83	4.11	4.00	4.31	1.86	3.45	3.53	3.40	1.3	1.20	1.35	3.44	2.99	3.47
FeO	2.20	2.67	2.72	2.66	2.74	2.75	2.86	2.55	2.62	2.60	2.22	1.93	2.28	2.44	2.25	2.17	2.26
MnO	0.10	0.07	0.06	0.00	0.13	0.09	0.14	0.03	0.09	0.09	0.00	0.03	0.03	0.07	0.08	0.10	0.00
NiO	0.07	0.06	0.05	0.09	n.a.	n.a.	n.a.	n.a.	n.a.	n.a.	0.11	0.08	0.06	0.07	0.00	0.00	0.02
MgO	17.66	18.84	18.58	16.98	17.44	17.04	16.91	18.29	18.28	17.77	17.53	17.30	17.36	17.63	16.84	17.26	16.68
CaO	24.24	22.15	22.28	23.12	22.69	22.78	22.83	23.22	21.51	22.69	22.58	23.82	23.47	23.13	23.49	23.59	22.57
Na_2O	0.04	0.07	0.04	0.10	0.06	0.06	0.06	0.05	0.05	0.05	0.06	0.11	0.12	0.07	0.20	0.15	0.48
K_2O	<0.01	0.01	<0.01	<0.01	0.02	<0.01	0.01	<0.01	<0.01	<0.01	0.01	<0.01	0.02	<0.01	<0.01	<0.01	0.01
Total	100.78	100.28	100.75	100.84	100.72	100.55	100.10	100.32	100.14	100.74	99.75	100.14	100.72	100.94	100.18	100.02	99.80
Si	1.886	1.902	1.920	1.906	1.879	1.891	1.873	1.943	1.913	1.902	1.906	1.928	1.923	1.920	1.903	1.911	1.915
Ti	0.001	0.000	0.001	0.001	0.000	0.002	0.001	0.002	0.001	0.001	0.001	0.001	0.001	0.001	0.004	0.004	0.004
Cr	0.038	0.035	0.030	0.033	0.045	0.044	0.046	0.016	0.034	0.035	0.042	0.084	0.094	0.092	0.040	0.033	0.045
Al	0.133	0.118	0.113	0.163	0.175	0.171	0.185	0.079	0.147	0.150	0.146	0.049	0.051	0.058	0.147	0.128	0.149
Fe	0.067	0.081	0.082	0.080	0.083	0.083	0.087	0.077	0.079	0.079	0.068	0.059	0.069	0.074	0.068	0.066	0.069
Mn	0.003	0.002	0.002	0.000	0.004	0.003	0.004	0.001	0.003	0.003	0.000	0.001	0.001	0.002	0.002	0.003	0.000
Ni	0.002	0.002	0.001	0.003	n.a.	n.a.	n.a.	n.a.	n.a.	n.a.	0.003	0.002	0.002	0.002	0.000	0.000	0.001
Mg	0.955	1.018	0.998	0.913	0.94	0.92	0.92	0.9	0.98	0.96	0.951	0.942	0.941	0.953	0.91	0.94	0.905
Ca	0.942	0.861	0.860	0.893	0.880	0.884	0.892	0.900	0.833	0.877	0.881	0.933	0.915	0.899	0.915	0.920	0.880
Na	0.003	0.005	0.003	0.007	0.014	0.014	0.014	0.014	0.014	0.003	0.014	0.008	0.008	0.005	0.014	0.011	0.034
K	0.000	0.000	0.000	0.000	0.001	0.000	0.000	0.000	0.000	0.000	0.000	0.000	0.001	0.000	0.000	0.000	0.001
Cat	4.029	4.024	4.009	3.999	4.013	4.002	4.013	4.009	3.998	4.006	4.001	4.008	4.008	4.006	4.007	4.011	4.002
Mg#	0.93	0.93	0.92	0.92	0.92	0.92	0.91	0.93	0.93	0.92	0.93	0.94	0.93	0.93	0.93	0.93	0.93

(*continued on next page*)

3c (*continued*)

Mineral	Orthopyroxene (normalized to 6 oxygens)																
Sample	OD 22 o22z3op2	OD 26 o26c2op1	OD 28 o28c1op7	OD 28 o28c2op1	OD 29 o29c2op1	OD 32 dp32op1	OD 32 dp32op1	OD 34 dp34op1	OD 34 dp34op3b	OD 38 dp38opc1	OD 38 dp38opc3	OD 42 42op2	OD 42 42op7	OD 48 48op1	OD 48 48op2	OD 48 48op5b	OD 52 odp52op4
SiO_2	56.08	55.47	55.39	55.75	56.09	56.41	56.74	54.88	56.16	55.79	56.58	56.03	55.62	56.09	55.59	56.73	56.12
TiO_2	<0.01	0.02	<0.01	0.01	0.01	0.01	0.03	0.02	0.02	0.03	0.01	<0.01	0.04	0.07	0.06	0.05	0.05
Cr_2O_3	0.80	0.68	0.73	0.86	0.66	0.86	2.17	0.66	0.86	0.82	1.05	2.44	2.54	2.66	2.82	2.08	0.87
Al_2O_3	2.13	2.10	2.24	2.22	2.29	0.77	0.44	3.05	2.80	3.40	2.96	0.78	0.76	0.86	0.84	0.51	2.57
FeO	6.38	5.47	5.52	5.52	5.25	6.13	6.21	5.12	5.14	5.64	0.00	5.63	6.03	5.31	5.63	5.77	5.16
MnO	0.13	0.12	0.14	0.09	0.17	0.15	0.13	0.13	0.18	0.13	6.01	0.18	0.19	0.11	0.10	0.18	0.06
NiO	0.10	0.14	0.12	0.08	0.13	0.06	0.08	0.09	0.08	0.13	0.03	0.10	0.10	0.13	0.15	0.06	0.15
MgO	33.49	34.68	34.20	34.14	32.62	33.73	34.65	32.95	33.68	32.07	0.18	33.58	33.62	33.47	33.82	34.55	33.53
CaO	1.76	1.50	2.01	1.63	2.75	1.67	0.99	1.80	1.14	2.01	32.69	1.71	1.42	1.86	1.29	0.88	1.34
Na_2O	<0.01	<0.01	0.01	<0.01	<0.01	<0.01	0.01	<0.01	<0.01	0.01	1.48	0.01	0.01	0.04	0.01	<0.01	0.03
K_2O	<0.01	0.01	<0.01	0.01	<0.01	0.01	0.02	<0.01	<0.01	<0.01	0.02	0.01	<0.01	<0.01	0.01	0.03	0.01
Total	100.86	100.19	100.38	100.30	100.26	101.66	101.47	98.70	100.06	100.03	101.02	100.47	100.33	100.60	100.32	100.84	99.88
Si	1.932	1.917	1.914	1.924	1.939	1.936	1.946	1.920	1.934	1.929	1.938	1.941	1.934	1.940	1.930	1.952	1.937
Ti	0.000	0.000	0.000	0.000	0.000	0.000	0.001	0.001	0.001	0.001	0.000	0.000	0.001	0.002	0.002	0.001	0.001
Cr	0.022	0.019	0.020	0.023	0.026	0.074	0.059	0.018	0.023	0.022	0.028	0.067	0.070	0.073	0.077	0.057	0.024
Al	0.087	0.086	0.091	0.090	0.093	0.031	0.018	0.126	0.114	0.139	0.0120	0.032	0.031	0.035	0.034	0.021	0.104
Fe	0.184	0.158	0.160	0.159	0.152	0.176	0.178	0.150	0.148	0.163	0.172	0.163	0.175	0.154	0.163	0.166	0.149
Mn	0.004	0.004	0.004	0.003	0.005	0.004	0.004	0.004	0.005	0.004	0.001	0.005	0.006	0.003	0.003	0.005	0.002
Ni	0.003	0.004	0.003	0.002	0.003	0.002	0.002	0.003	0.002	0.004	0.005	0.003	0.003	0.004	0.004	0.002	0.004
Mg	1.719	1.787	1.761	1.756	1.681	1.726	1.771	1.718	1.728	1.653	1.669	1.734	1.742	1.725	1.750	1.772	1.725
Ca	0.065	0.056	0.074	0.060	0.102	0.061	0.036	0.067	0.042	0.074	0.054	0.063	0.053	0.069	0.048	0.032	0.049
Na	0.000	0.000	0.001	0.000	0.000	0.000	0.001	0.000	0.000	0.001	0.002	0.001	0.001	0.003	0.001	0.000	0.002
K	0.000	0.000	0.000	0.000	0.000	0.000	0.001	0.000	0.000	0.000	0.000	0.000	0.000	0.000	0.000	0.001	0.000
Cat	4.014	4.030	4.030	4.019	4.001	4.011	4.016	4.007	3.997	3.990	3.989	4.010	4.015	4.006	4.013	4.009	3.998
Mg#	0.90	0.92	0.92	0.92	0.92	0.91	0.91	0.92	0.92	0.91	0.91	0.91	0.91	0.92	0.91	0.91	0.92

3d (*continued*)

Mineral	Spinel (normalized to 3 cations)																
Sample	OD 2 o2c5sp3	OD 06 o6c3sp4	OD 7 o7c1sp3	OD 15 o15c4sp2	OD 18 o18c5sp2	OD 26 o26c2sp1	OD 28 32spc1	OD 29 o29c4sp1	OD 32 dp32spc2	OD 32 dp32spc	OD 42 42sp3	OD 48 48sp1	OD 48 48sp5	OD 48 48sp1b	OD 48 48sp1	OD 48 48sp7	OD 49 dp49chr1
SiO_2	0.01	<0.01	<0.01	0.03	0.04	0.12	0.15	0.04	0.04	0.04	0.04	0.01	0.03	0.04	0.01	0.02	0.00
TiO_2	0.07	0.03	0.02	0.01	0.04	<0.01	0.02	0.05	0.05	0.05	0.08	0.13	0.12	0.09	0.13	0.17	0.05
Cr_2O_3	43.65	41.63	43.93	43.00	40.51	40.62	43.73	42.83	29.07	29.52	12.23	34.55	31.5	37.25	34.55	28.77	31.38
Al_2O_3	26.36	27.04	25.48	27.03	28.91	27.77	24.84	25.90	40.23	41.35	52.58	35.07	38.85	32.40	35.07	41.00	37.18
Fe_2O_3	2.84	2.53	2.15	2.18	2.31	3.44	3.29	2.70	2.48	1.04	4.41	1.48	1.14	1.16	1.48	0.89	3.00
FeO	13.47	13.70	13.85	13.81	13.75	13.59	13.94	13.70	12.90	14.16	24.84	13.11	14.33	12.80	13.11	14.85	15.33
MnO	<0.01	0.02	0.03	<0.01	<0.01	0.26	0.31	0.39	0.09	0.06	0.11	0.03	0.11	0.07	0.03	0.07	0.10
NiO	0.13	0.14	0.12	0.11	0.10	0.12	0.13	0.10	0.14	0.11	0.09	0.16	0.10	0.15	0.16	0.12	0.09
MgO	15.16	14.63	14.44	14.79	14.99	14.91	14.38	14.38	15.44	14.89	5.86	15.87	14.66	16.30	15.87	14.08	14.36
ZnO	n.a.	n.a.	n.a.	n.a.	n.a.	n.a.	n.a.	n.a.	0.10	0.12	0.14	0.17	0.20	0.16	0.17	0.17	n.a.
Total	101.69	99.71	100.02	101.00	100.70	100.86	100.79	100.11	100.59	101.37	100.39	100.62	100.62	100.48	100.62	100.17	101.52
Si	0.000	0.000	0.000	0.001	0.001	0.004	0.004	0.001	0.001	0.001	0.001	0.000	0.001	0.001	0.000	0.001	0.000
Ti	0.001	0.001	0.000	0.000	0.001	0.000	0.000	0.001	0.001	0.001	0.002	0.003	0.003	0.002	0.003	0.004	0.001
Cr	1.017	0.986	1.046	1.007	0.943	0.949	1.038	1.018	1.007	1.017	0.485	1.168	1.071	1.244	1.168	1.009	1.076
Al	0.916	0.955	0.904	0.944	1.003	0.968	0.879	0.917	0.934	0.956	1.398	0.795	0.899	0.726	0.795	0.964	0.856
Fe_3	0.063	0.057	0.049	0.049	0.051	0.076	0.074	0.061	0.055	0.023	0.112	0.032	0.025	0.025	0.032	0.020	0.066
Fe_2	0.332	0.343	0.349	0.342	0.339	0.336	0.350	0.344	0.317	0.346	0.699	0.315	0.351	0.303	0.315	0.369	0.373
Mn	0.000	0.001	0.001	0.000	0.000	0.007	0.008	0.010	0.003	0.003	0.003	0.004	0.002	0.004	0.004	0.003	0.003
Ni	0.003	0.003	0.003	0.003	0.002	0.003	0.003	0.002	0.002	0.003	0.002	0.004	0.004	0.003	0.004	0.004	0.002
Mg	0.666	0.654	0.648	0.653	0.658	0.657	0.643	0.644	0.676	0.649	0.294	0.678	0.640	0.688	0.678	0.624	0.623
ZnO	n.a.	n.a.	n.a.	n.a.	n.a.	n.a.	n.a.	n.a.	0.002	0.002	0.003	0.004	0.005	0.004	0.004	0.004	n.a.
Cat	3.000	3.000	3.000	3.000	3.000	3.000	3.000	3.000	3.000	3.000	3.000	3.000	3.000	3.000	3.000	3.000	3.000
Mg#	0.63	0.62	0.62	0.63	0.63	0.61	0.60	0.61	0.65	0.64	0.29	0.66	0.63	0.68	0.66	0.62	0.59
Cr#	0.53	0.51	0.54	0.52	0.48	0.50	0.54	0.53	0.33	0.32	0.70	0.40	0.35	0.44	0.40	0.32	0.36

(*continued on next page*)

3e (*continued*)

Mineral	**Magnetite (normalized to 3 cations)**						
Sample	OD2	OD 6	OD 7	OD 15	OD 18	OD 42	OD 48
	o2c2mt1	o6c2sp2	o7c1mt1	o15c3mt2	odp18c4π	42sp6	48mag1
SiO_2	0.75	0.73	1.02	0.57	0.77	0.07	1.06
TiO_2	<0.01	0.02	<0.01	<0.01	<0.01	0.27	0.01
Cr_2O_3	0.01	0.02	0.51	0.02	2.30	0.08	0.02
Al_2O_3	0.01	0.01	0.02	0.00	0.00	6.55	0.00
Fe_2O_3	67.04	67.89	66.36	66.04	64.44	61.22	67.23
FeO	30.62	31.76	32.19	30.77	31.55	32.32	29.96
MnO	0.42	0.14	0.13	0.16	<0.01	<0.01	0.25
NiO	0.12	0.01	0.03	0.03	<0.01	0.09	0.04
MgO	0.45	0.09	0.09	0.06	0.20	0.25	1.24
Total	**99.43**	**100.74**	**100.39**	**97.68**	**99.27**	**100.86**	**99.89**
Si	0.029	0.028	0.039	0.023	0.030	0.003	0.040
Ti	0.000	0.001	0.000	0.000	0.000	0.007	0.000
Cr	0.000	0.001	0.015	0.001	0.070	0.002	0.001
Al	0.001	0.000	0.001	0.000	0.000	0.284	0.000
Fe^{3+}	1.941	1.945	1.906	1.954	1.870	1.694	1.922
Fe^{2+}	0.985	1.011	1.027	1.012	1.018	0.994	0.952
Mn	0.014	0.005	0.004	0.005	0.000	0.000	0.008
Ni	0.004	0.000	0.001	0.001	0.000	0.003	0.001
Mg	0.026	0.005	0.005	0.003	0.011	0.014	0.070
Cat	**3.000**	**3.000**	**3.000**	**3.000**	**3.000**	**3.000**	**3.000**

chlorite (normalized to 18 oxygens)		
Sample	OD 42	OD 42
	42ch1	42ch2
SiO_2	34.07	33.37
TiO_2	0.03	0.01
Cr_2O_3	12.78	14.10
Al_2O_3	1.21	0.48
FeO	5.05	5.26
MnO	0.02	0.00
MgO	33.38	33.11
CaO	0.02	0.01
Na_2O	0.02	0.01
K_2O	0.04	0.03
Cl	0.03	0.01
H_2O	12.52	12.51
Total	**99.17**	**98.89**
Si	3.26	3.20
Ti	0.00	0.00
Al	1.44	1.59
Cr	0.09	0.04
Fe	0.40	0.42
Mn	0.00	0.00
Mg	4.76	4.73
Ca	0.00	0.00
Na	0.00	0.00
K	0.00	0.00
Cl	0.00	0.00
H	8.00	8.00
Cat	**17.97**	**17.99**

phlogopite (normalized to 11) oxygens		
Sample	OD 42	OD 42
	42bt1	42bt2
SiO_2	41.89	43.55
TiO_2	0.19	0.23
Cr_2O_3	1.26	1.35
Al_2O_3	12.17	12.23
FeO	4.64	3.97
MnO	0.05	0.02
MgO	25.71	25.58
CaO	0.03	0.03
Na_2O	0.21	0.21
K_2O	8.37	8.35
Cl	0.03	0.07
H_2O	4.60	4.62
Total	**99.30**	**100.55**
F,Cl=O	**0.04**	**0.09**
Total	**99.26**	**100.46**
Si	2.70	2.76
Ti	0.01	0.01
Cr	0.06	0.07
Al	0.93	0.91
Fe	0.25	0.21
Mn	0.00	0.00
Mg	2.47	2.42
Ca	0.00	0.00
Na	0.03	0.03
K	0.69	0.68
Cl	0.02	0.04
H	1.98	1.96
Cat	**7.15**	**7.09**

3f (*continued*)

Mineral	Serpentine (normalized to 9 oxygens)									Serpentine matrix (normalized to 9 oxygens)						
Sample	OD 6 o6c2s13	OD 7 o7c1sr1	OD 7 o7c5sr9	OD 11 O11c2sr2	OD 18 o18c4sr25	OD 22 o22z5sr7a	OD 26 o26c3sr1	OD 28 o28c2sr4	OD 29 o29c5sr5	OD 2 o2c5sr8	OD 11 o11c5s10	OD 15 o15c1sr3	OD 15 o15c1sr10	OD 18 o18c5sr12	OD 22 o22z3sr3	OD 26 o26c3sr7
SiO_2	40.38	39.26	42.02	40.94	40.89	40.41	40.57	40.00	39.06	37.47	35.33	35.89	38.75	36.52	38.77	36.56
TiO_2	<0.01	0.01	0.01	<0.01	0.01	<0.01	<0.01	0.03	<0.01	0.03	<0.01	0.01	0.01	0.02	0.01	0.01
Cr_2O_3	0.02	0.71	0.02	<0.01	0.03	<0.01	0.01	<0.01	0.81	0.99	<0.01	0.01	0.71	<0.01	0.74	<0.01
Al_2O_3	0.03	1.20	0.24	0.07	0.11	0.95	0.64	0.89	1.48	0.60	0.23	0.28	1.77	0.36	1.77	0.26
FeO	4.85	4.82	2.83	3.30	3.87	5.31	2.58	5.49	5.70	5.89	2.93	1.86	4.69	3.03	6.31	3.81
MnO	0.11	0.14	0.01	0.05	0.01	0.05	0.09	0.12	0.15	0.09	0.07	0.05	0.13	<0.01	0.18	0.06
NiO	0.43	0.16	0.05	0.44	0.35	<0.01	<0.01	0.02	0.07	0.07	0.12	0.04	0.01	<0.01	<0.01	0.05
MgO	40.08	36.79	40.73	40.43	38.84	38.49	40.13	37.67	37.05	35.74	33.80	34.96	36.59	35.19	35.93	34.82
CaO	0.02	0.03	0.04	0.02	0.01	0.02	0.03	0.03	0.07	0.03	0.01	0.01	0.03	0.02	0.05	0.03
Na_2O	0.06	0.09	0.04	0.04	0.04	0.02	<0.01	0.02	<0.01	0.07	0.12	0.07	0.05	0.03	<0.01	0.01
K_2O	<0.01	0.01	<0.01	0.01	0.01	0.01	0.01	<0.01	<0.01	<0.01	0.01	<0.01	<0.01	0.01	0.01	<0.01
Cl	1.34	1.13	1.23	0.47	0.45	0.38	1.08	0.94	1.36	1.41	2.56	3.62	1.12	2.57	0.67	0.70
H_2O	12.09	11.77	12.34	12.35	12.18	12.28	12.09	11.97	11.82	11.26	9.99	9.88	11.72	10.38	11.87	10.86
Total	99.42	96.12	99.56	98.11	96.80	97.92	97.24	97.18	97.56	93.66	85.17	86.67	95.56	88.11	96.31	87.16
Cl=O	0.30	0.25	0.28	0.11	0.10	0.08	0.24	0.21	0.31	0.32	0.58	0.82	0.25	0.58	0.15	0.16
Total	99.11	95.86	99.28	98.01	96.70	97.83	96.99	96.97	97.27	93.34	84.59	85.85	95.31	87.54	96.15	87.01
Si	1.947	1.953	1.991	1.970	1.995	1.959	1.967	1.965	1.926	1.934	1.991	1.992	1.936	1.986	1.930	1.987
Ti	0.000	0.000	0.000	0.000	0.000	0.000	0.000	0.001	0.000	0.001	0.000	0.000	0.000	0.001	0.000	0.000
Cr	0.001	0.028	0.001	0.000	0.001	0.000	0.000	0.000	0.032	0.040	0.000	0.000	0.028	0.000	0.029	0.000
Al	0.002	0.070	0.013	0.004	0.006	0.054	0.037	0.051	0.086	0.036	0.015	0.018	0.104	0.023	0.104	0.017
Fe	0.196	0.200	0.112	0.133	0.158	0.215	0.105	0.225	0.235	0.254	0.138	0.086	0.196	0.138	0.263	0.173
Mn	0.004	0.006	0.000	0.002	0.000	0.002	0.004	0.005	0.006	0.004	0.003	0.002	0.006	0.000	0.008	0.003
Ni	0.017	0.006	0.002	0.017	0.014	0.000	0.000	0.001	0.003	0.003	0.005	0.002	0.000	0.000	0.000	0.002
Mg	2.881	2.727	2.877	2.899	2.824	2.781	2.900	2.757	2.723	2.749	2.840	2.892	2.725	2.852	2.666	2.820
Ca	0.001	0.002	0.002	0.001	0.001	0.001	0.002	0.002	0.004	0.002	0.001	0.0010	0.001	0.001	0.002	0.001
Na	0.006	0.009	0.004	0.004	0.004	0.002	0.000	0.002	0.000	0.007	0.013	0.008	0.004	0.003	0.000	0.001
K	0.000	0.001	0.000	0.001	0.001	0.000	0.000	0.000	0.000	0.000	0.001	0.000	0.000	0.000	0.001	0.000
Cl	0.110	0.095	0.099	0.038	0.037	0.031	0.089	0.078	0.113	0.124	0.224	0.340	0.095	0.237	0.057	0.064
Cat	5.054	5.002	5.003	5.030	5.004	5.015	5.015	5.009	5.015	5.030	5.008	5.002	5.000	5.004	5.003	5.005

H_2O calculated assuming stoichiometry.

Table 4
Representative light element contents of minerals from the two drill sites

Site 1272A	Li		Be		B	
	μg g^{-1}	1σ	ng g^{-1}	1σ	μg g^{-1}	1σ
Olivine						
OD29Cloll	0.98	0.05	0.000	0.62	0.00	0.00
OD29Clol2	0.90	0.05	b.d.l.	—	0.00	0.01
OD26C3ol2	0.67	0.05	0.75	1.31	0.00	0.01
OD26C3ol3	0.68	0.08	0.75	1.31	0.01	0.01
OD28Cloll	0.52	0.06	0.56	0.91	0.00	0.01
OD28C3ol3	0.61	0.04	2.54	5.35	0.01	0.01
OD6C2oll	1.04	0.04	b.d.l.	—	0.01	0.01
OD2Cloll	0.89	0.05	0.98	2.08	0.03	0.02
Orthopyroxene						
OD22C4op2	0.67	0.03	0.22	0.23	0.02	0.01
OD22C3oppl-l	0.72	0.07	0.80	1.42	0.00	0.01
OD22C3opp1-2	0.69	0.13	1.03	1.33	0.01	0.01
OD22C3opp1-3	0.56	0.06	0.64	1.25	0.01	0.01
OD22C3opp1-4	0.80	0.37	1.93	4.00	0.01	0.01
OD22C3opp1-5	0.54	0.05	0.63	0.90	0.00	0.00
OD22C3opp1-6	0.78	0.16	0.13	0.42	0.00	0.00
OD29C5op1	0.76	0.04	1.19	1.17	0.02	0.01
OD26C4op2	0.95	0.03	0.16	0.49	0.01	0.01
OD26C3op3	0.72	0.04	0.16	0.50	0.00	0.00
OD26C3op2	0.80	0.07	0.50	0.81	0.00	0.01
OD28C2op6	0.61	0.03	0.99	1.39	0.01	0.01
OD28C1op3	1.00	0.04	0.50	0.81	0.16	0.02
Clinopyroxene						
OD29C2cp4	5.41	0.23	0.16	0.50	0.93	0.13
OD29C2cp5	4.39	0.20	0.67	1.17	2.39	0.19
OD29C2cp1	2.69	0.04	0.22	0.29	0.74	0.7
OD28C2cp2	1.56	0.07	0.91	1.17	0.041	0.01
OD28Clcp5	2.14	0.10	b.d.l.	—	0.04	0.01
Serpentine minerals						
OD7C9srlO	0.05	0.01	0.25	0.53	39.29	0.55
OD7C5sr11	0.11	0.01	0.70	1.22	14.79	0.29
OD26C3sr2	0.44	0.02	1.29	1.52	58.10	2.90
OD28C2sr15	2.09	0.03	0.30	0.70	71.38	2.33
OD28C1sr8	1.80	0.06	0.49	0.79	138.20	3.16
OD11C5sr11	0.07	0.01	0.27	0.57	37.94	0.02
OD6C1sr4	0.01	0.01	0.70	1.23	38.94	1.13
OD7C3sr8	0.22	0.2	0.27	0.57	84.57	2.16
OD11C2sr5	0.19	0.02	0.16	0.52	52.77	1.95
OD6C3sr4	0.00	0.00	0.38	0.62	31.56	0.56
OD7C1sr14	0.02	0.01	0.22	0.46	24.14	0.52
OD7C3sr1	0.22	0.03	0.13	0.42	80.50	2.31
OD11C5sr9	0.03	0.01	0.39	0.63	12.92	0.34
OD22C3srl	0.01	0.00	0.43	0.95	20.0	1.03
OD2C2srl0	0.03	0.01	0.77	0.95	37.08	0.76
OD2C2sr31	0.39	0.04	0.38	0.76	72.42	3.41
OD2C3sr7	0.07	0.02	0.53	0.81	13.76	0.53
OD2C5srll	0.06	0.01	b.d.l.	—	65.10	0.95
OD15C2sr7	0.19	0.01	0.34	0.67	76.13	0.84
OD15C1sr6	0.00	0.00	0.18	0.55	35.00	0.68
OD15C1sr10	0.27	0.04	0.20	0.61	92.51	1.17
OD15C3sr4	0.18	0.03	0.20	0.59	27.72	0.31
OD15C3srll	1.61	0.09	b.d.l.	—	101.53	2.09
OD18C2sr8	1.50	0.16	b.d.l.	—	83.73	1.59
ODP18C2sr5	0.62	0.04	0.87	1.06	88.89	2.84
OD6C1sr1	0.03	0.27	0.32	2.11	37.58	0.034
OD6C1sr5	0.21	0.6	0.54	4.1	74.1	0.045
OD6C1sr6	0.07	0.16	0.31	2.11	33.54	0.016

Table 4 (*continued*)

Site 1274A	Li		Be		B	
	μg g^{-1}	1σ	ng g^{-1}	1σ	μg g^{-1}	1σ
Olivine						
OD32oli-1	0.86	0.03	0.42	0.83	0.00	0.00
OD34oli2	0.81	0.04	0.49	0.62	0.01	0.00
OD34oli3	1.15	0.04	0.00	0.00	0.02	0.01
OD38ol-1	0.85	0.04	0.22	0.44	0.01	0.00
OD38ol-4	1.02	0.04	0.22	0.43	0.02	0.01
OD42oli-1	1.30	0.04	0.48	0.49	0.00	0.00
OD42oli-4	1.04	0.02	0.61	0.68	0.01	0.00
OLII-42oli-5	8.29	0.09	9.87	2.92	0.55	0.04
OD48oli-2	0.94	0.02	0.60	0.92	0.04	0.02
OD52ol1	0.88	0.03	0.56	0.71	0.00	0.00
OD52olb1	0.76	0.03	0.29	0.55	0.01	0.00
Orthopyroxene						
OD52opxb2	0.61	0.02	3.64	1.57	0.08	0.02
OD52opxb3	0.65	0.03	2.76	1.43	0.01	0.00
OD34opxb1	0.60	0.01	0.43	0.54	0.01	0.00
OD34opxb2	0.48	0.03	0.90	0.95	0.01	0.01
OD34opxc1	0.67	0.04	0.42	0.53	0.01	0.00
OD38opx-1	0.83	0.03	0.94	0.84	0.01	0.01
OD48opx-3	0.39	0.02	0.25	0.34	0.01	0.00
OD32opxI-1	0.61	0.02	0.55	0.56	0.01	0.00
Clinopyroxene						
OD32cpxI-l	1.56	0.05	0.50	0.71	0.05	0.01
OD32cpxI-2	1.42	0.07	0.22	0.44	0.10	0.02
OD34cpxcl	2.80	0.08	1.30	1.51	0.01	0.01
OD34cpxc3	0.45	0.02	0.83	0.65	0.01	0.01
OD38cpx-1	1.56	0.05	0.75	0.77	0.03	0.01
OD38cpx-2	1.70	0.04	1.38	1.98	0.81	0.06
OD42cpx-4	2.02	0.05	67.38	7.29	0.12	0.03
OD48cpx-4	1.29	0.03	0.96	0.52	1.88	0.05
OD52cpx3	1.51	0.06	5.43	2.06	0.01	0.01
Serpentine minerals						
OD32ba-2	0.59	0.02	0.69	0.85	9.53	0.27
OD34ba3	9.38	0.16	0.46	0.58	58.10	0.81
OD42ba-3	0.90	0.02	15.72	2.95	1.46	0.11
OD48ba-1	2.08	0.26	0.65	0.58	63.04	3.80
OD49ba-1	0.19	0.01	0.26	0.34	50.21	0.39
OD52ba3	0.43	0.02	6.13	2.30	69.57	0.61
OD38ba-3	0.19	0.02	0.39	0.79	21.64	0.17
OD38ba-5	1.23	0.05	0.21	0.41	40.58	0.51
OD42se-1	0.05	0.00	1.93	0.82	4.28	0.20
OD42ser-4	0.20	0.02	3.44	0.0	0.09	0.02
OD38ser-3	0.10	0.01	0.60	0.61	11.65	0.13
OD38ser-4	0.12	0.01	b.d.l.	—	3.81	0.15
OD32sol-2	0.09	0.01	b.d.l.	—	0.44	0.12
OD48ser-l	0.08	0.01	0.12	0.25	9.96	0.15
OD48sv-2	0.64	0.02	2.21	1.82	14.02	0.24
OD52sev2	0.09	0.01	0.00	0.00	24.45	0.22
OD52sev4	0.13	0.02	0.90	0.94	40.39	0.47
OD32serol-1	0.12	0.01	0.35	0.46	2.85	0.56
Chrysotile vein						
OD32chry-2	0.37	0.03	0.96	0.86	15.54	0.24
OD34chry2	0.29	0.02	0.24	0.45	20.08	0.36
OD42chry-1	0.11	0.01	0.88	0.54	4.04	0.11
OD48chry-l	0.14	0.02	0.51	1.02	24.10	0.91
OD49chry-2	0.08	0.01	1.85	1.68	19.33	1.42
OD52chry2	0.07	0.01	0.64	0.62	26.04	0.14
OD52chry4	0.07	0.01	0.45	0.57	26.25	0.27

1σ showed as example of measurement errors (b.d.l., below dedection limit; OD2c29cp1, sample OD 2; circle 2 cpx grain 4). Detection limits are: 1.4 ng/g (Li), 1.0 ng/g (Be), 7.5 ng/g (B).

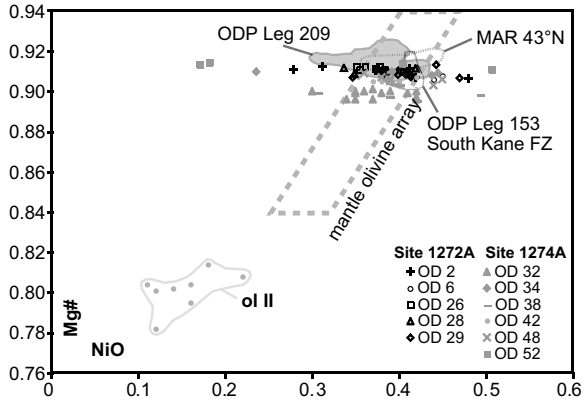

Fig. 4. NiO versus Mg#-diagram showing olivine compositions from ODP Leg 209 Sites 1272A and 1274A. Mantle olivine array after Takahashi et al. (1987). MAR 43° after Shibata and Thompson (1986). ODP Leg 153 data after Ross and Elthon (1997); ODP Leg 209 data after Moll et al. (2007).

samples are 0.67 μg g^{-1} Li, 48.29 μg g^{-1} B, and 4.5 ng g^{-1} Be (Table 4).

5.1.3. Accessory minerals

Spinel has Cr# (Cr# = Cr/[Cr + Al]) between 0.37 and 0.54 and Mg# from 0.55 to 0.68 (Fig. 7). In sample OD 42, spinel has higher Cr# (0.70) and lower Mg# (0.29). TiO_2 values are below 0.2 wt%. Fe_2O_3 in magnetite varies from 61.2 to 67.9 wt%. Small grain size led to some SiO_2 contamination. Chlorite has Mg# 0.92 and Cr_2O_3 contents of <1.2 wt%. The light element contents of the two mineral grains analyzed are 0.40 μg g^{-1} and 0.53 μg g^{-1} for Li, 44.9 ng g^{-1} and 61.3 ng g^{-1} for Be and 0.97 μg g^{-1} and 0.85 μg g^{-1} for B. The mica (coexisting with magmatic olivine) in OD 42 is a phlogopite with Mg# of 0.91.

5.2. Light element, H_2O and Cl contents of whole rock samples

As only little material was available, only limited whole rock analysis for B, H and Cl by PGAA could be performed (Table 5, Fig. 8). Li concentrations in some samples are available from isotope dilution (data from Vils et al., 2008).

PGAA measures of B whole rock contents range from 50.3 μg g^{-1} to 65 μg g^{-1} at Site 1272A and from 10.4 μg g^{-1} to 38.5 μg g^{-1} at Site 1274A. H_2O contents of whole rock samples determined by PGAA vary between 13.0 and 16.4 wt% at Site 1272A, and from 10.9 to 15.0 wt% at Site 1274A. Cl whole rock contents determined by PGAA range from 6032 to 10,114 μg g^{-1} at Site 1272A and from 1061 to 3566 μg g^{-1} at Site 1274A (Table 5). Li content of whole rock determined by isotope dilution varies between 0.07 and 0.81 μg g^{-1} at Site 1272A, and between 0.28 and 3.37 μg g^{-1} at Site 1274A (data from Vils et al., 2008).

Calculated Li and B contents of whole rock samples based on mineral modes, in-situ measurements on minerals (this study) and spinel data from Ottolini et al. (2004; 0.51 μg g^{-1} for Li and 0.0035 μg g^{-1} for B), show no systematic deviation from measured values towards higher or lower values. Seventy percent of all analyzed samples are within an error of 20% (B) and 50% for Li, respectively. The low abundance of Li-bearing phases in ODP Leg 209 (only clinopyroxene) leads to a large uncertainty when calculating whole rock Li content.

Whole rock samples were not analyzed for Be. Due to the low abundance of this element found during the in-situ mineral analyses, we conclude that there is negligible Be in the serpentinized oceanic mantle.

The down-hole variation of B, Li, Cl and H_2O is illustrated in Fig. 8. At Site 1274, B, Cl and H_2O contents are generally higher at depth, although there is no clear correlation. The Li content remains more or less constant with

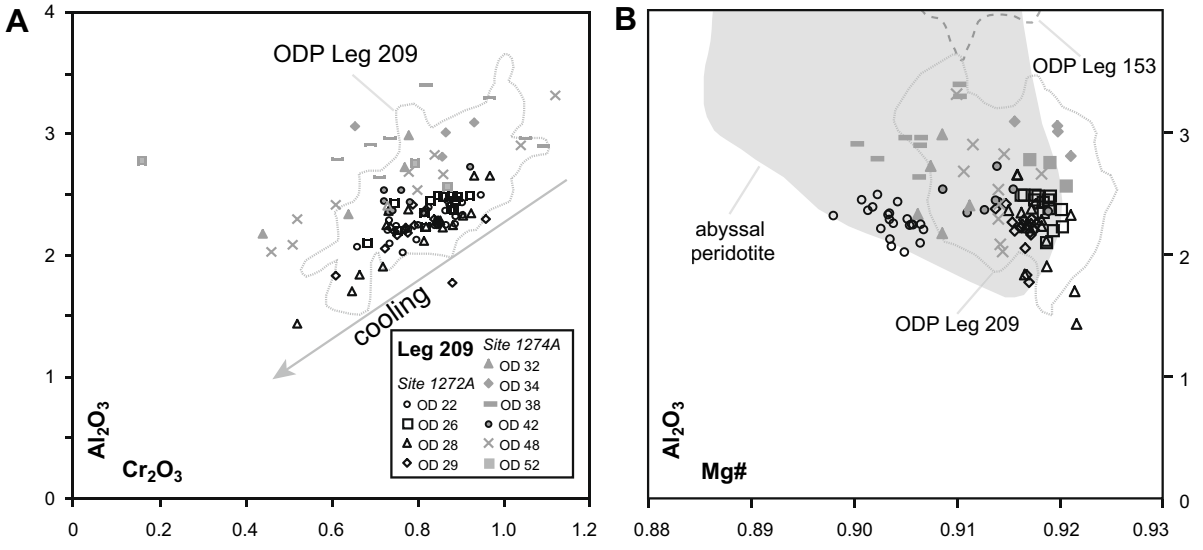

Fig. 5. (A) Al_2O_3 versus Cr_2O_3 diagram of orthopyroxene from ODP Leg 209, Sites 1272A and 1274A. (B) Mg# versus Al_2O_3 diagram. Abyssal peridotite field and ODP Leg 153 data after Ross and Elthon (1997). ODP Leg 209 data field after Seyler et al. (2007) and Moll et al. (2007).

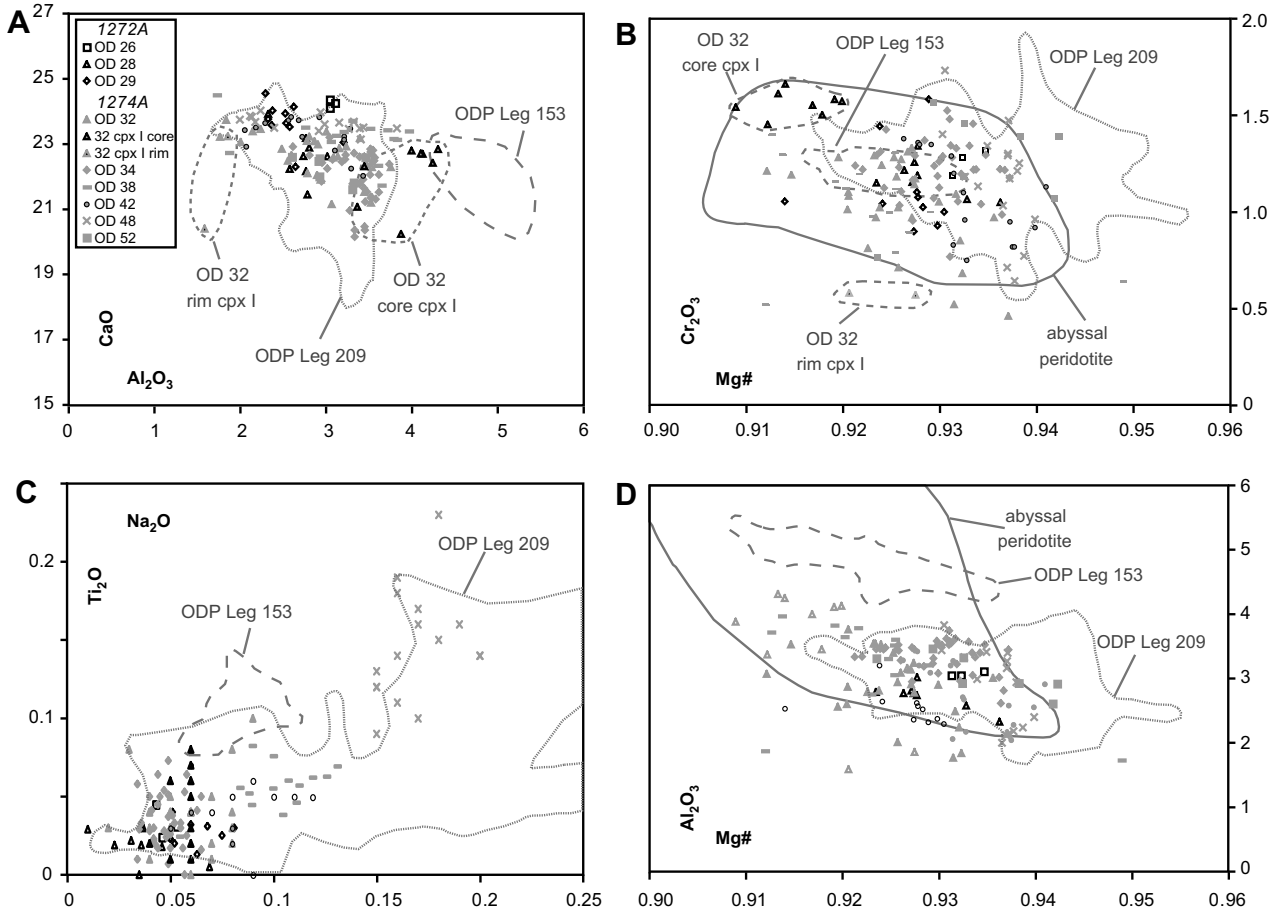

Fig. 6. Major element composition of clinopyroxene, core and rim of primary clinopyroxene (cpxI) are indicated as fields delimited by dashed lines. (A) Al_2O_3 versus CaO diagram, with data from ODP Leg 153 for comparison (MARK area). (B) Cr_2O_3 versus Mg# diagram. (C) Ti_2O versus Na_2O diagram. (D) Al_2O_3 versus Mg# diagram. Abyssal peridotites field after Ross and Elthon (1997), and references therein. ODP Leg 209 field after Seyler et al. (2007) and Moll et al. (2007).

depth. At Site 1272A, H_2O tends to lower values with depth, B may display a similar trend, while Li contents clearly increase with depth. The Cl whole rock content seems to decrease with depth from 10,000 to 6000 $\mu g\ g^{-1}$ and then remains roughly constant.

6. DISCUSSION

In the following, we will discuss the nature of the protoliths, including chemical and textural evidence of melt infiltration. Then, we will examine the impact of serpentinization on the B and Li contents of whole rock samples and present a model of the light element budget of the oceanic lithosphere.

6.1. Light element contents of primary minerals

Primary olivine of both ODP Sites shows Mg# between 0.90 and 0.92 (except sample OD 42), which is within the range of mantle olivine. This variation does not correlate with NiO contents, the latter varying at any given Mg. The Cr–Al systematics of orthopyroxene (Fig. 5b) and the Ca–Al–Cr systematics of clinopyroxene (Fig. 5a) are in line with those of other abyssal peridotites (e.g. Shibata and Thompson, 1986; Ross and Elthon, 1997). Spinel compositions are also concordant with values for abyssal peridotites (Fig. 7), except for a weak shift towards lower Mg#. This trend could be explained by partial diffusive re-equilibration to magnetite formed during serpentinization or upon cooling after melt infiltration (see section 'Protoliths and melt refertilization').

Light element contents of olivine and orthopyroxene (Table 4, Fig. 9) are close to the depleted mantle values reported by Salters and Stracke (2004). There is no trend for Li and B towards or away from seawater composition (4.6 $\mu g\ g^{-1}$ B, 0.18 $\mu g\ g^{-1}$ Li; Quinby-Hunt and Turekian, 1983; Jean-Baptise et al., 1991; Schmidt et al., 2007). The B and Li contents obtained in this study are also similar to those of olivine and orthopyroxene from the Pindos ophiolite, Greece (Pelletier, 2008). In contrast, B and Li in clinopyroxene show a wider range of values that trend towards the MORB field (Fig. 9, Ryan and Langmuir, 1987; Ryan and Langmuir, 1993), confirming that clinopyroxene probably crystallized later than primary olivine, orthopyroxene and spinel (see below). In summary, major, minor and light element composition of pyroxenes, spinel and the Mg# of oliv-

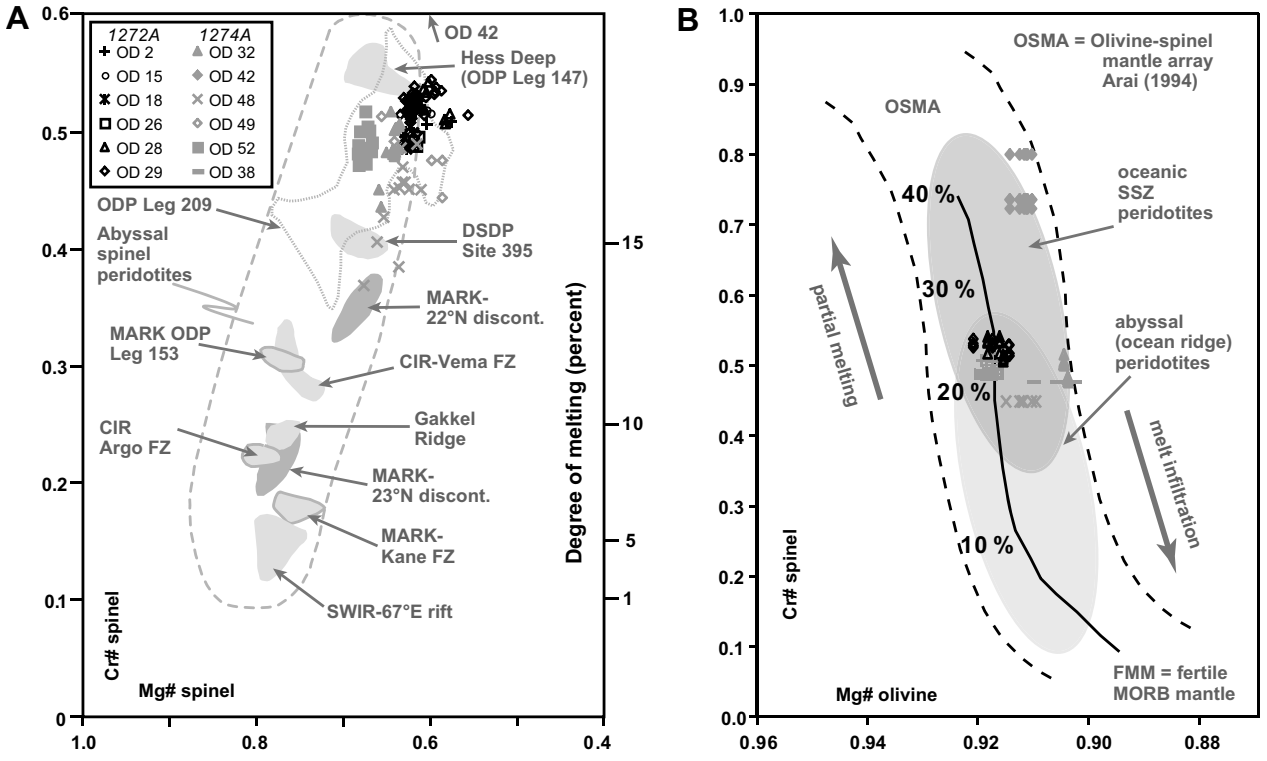

Fig. 7. (A) Cr# (=Cr/Cr + Al) versus Mg# (=Mg/(Mg + Fe_{tot}) diagram for spinel, modified after Hellebrand et al. (2002), showing the relative depletion of the mantle at ODP Leg 209. ODP Leg 209 field after Seyler et al. (2007) and Moll et al. (2007). (B) Cr# in spinel versus Mg# in olivine diagram, modified after Pelletier (2008) and references therein. OSMA, Olivine–spinel mantle array (after Arai, 1994); FMM, fertile MORB mantle (after Arai, 1994); and SSZ, supra subduction zone.

Table 5
Whole rock PGAA analyses from ODP leg 209

	SiO_2		H_2O		H		B		S		Cl	
	wt%	±	wt%	±	wt%	±	μg g^{-1}	±	μg g^{-1}	±	μg g^{-1}	±
Site 1272A												
OD 2	33.85	*0.90*	16.13	*0.43*	1.80	*0.04*	58.7	*1.11*		*0*	10114	*446*
OD 6	35.73	*0.93*	15.42	*0.41*	1.73	*0.04*	60.3	*1.10*	1380	*84*	7759	*343*
OD 11	35.10	*0.92*	16.40	*0.43*	1.84	*0.04*	53.9	*1.01*	1353	*107*	6389	*291*
OD 15	35.77	*0.93*	15.11	*0.40*	1.69	*0.04*	59.3	*1.08*	1330	*96*	6682	*314*
OD 18	35.84	*0.94*	15.34	*0.41*	1.72	*0.04*	59.8	*1.12*	1909	*132*	6355	*251*
OD 22	36.21	*0.92*	15.17	*0.40*	1.70	*0.04*	65.0	*1.18*	1402	*118*	7291	*289*
OD 26	30.64	*1.03*	13.00	*0.43*	1.45	*0.03*	61.5	*1.12*	2229	*74*	6032	*244*
OD 29	36.48	*0.94*	13.79	*0.37*	1.54	*0.03*	50.3	*0.92*	1399	*109*	6855	*247*
Site 1274A												
OD 34	36.74	*0.94*	12.75	*0.34*	1.43	*0.03*	31.2	*0.59*	781	*80*	2242	*90*
OD 38	37.30	*0.94*	13.12	*0.35*	1.47	*0.03*	17.5	*0.33*	825	*66*	2746	*129*
OD 42	36.33	*0.92*	13.82	*0.37*	1.55	*0.03*	<0.2	–	561	*66*	1553	*33*
OD 45	38.50	*0.98*	10.90	*0.30*	1.22	*0.03*	10.4	*0.20*	<500	–	1061	*44*
OD 48	37.50	*0.95*	12.20	*0.33*	1.37	*0.03*	38.5	*0.72*	<500	–	1823	*77*
OD 49	34.57	*0.92*	14.99	*0.40*	1.68	*0.04*	36.6	*0.69*	1056	*79*	3566	*144*

ine were not changed by serpentinization and can be used to constrain the peridotitic protolith of the serpentinites.

6.2. Protoliths and melt refertilization

It is commonly accepted that the spectrum of mantle rock samples at mid-ocean ridges has been produced by partial melting of the upper mantle at spinel-facies conditions, followed by removal of basaltic melt (e.g. Hamlyn and Bonatti, 1980; Dick and Bullen, 1984). The degree of partial melting can be deduced from the Cr# of spinel (Hellebrand et al., 2001), and spinel compositions from mantle rocks along the MAR suggest partial melting between 7% and 20% (Fig. 7a). Spinel in the studied samples from

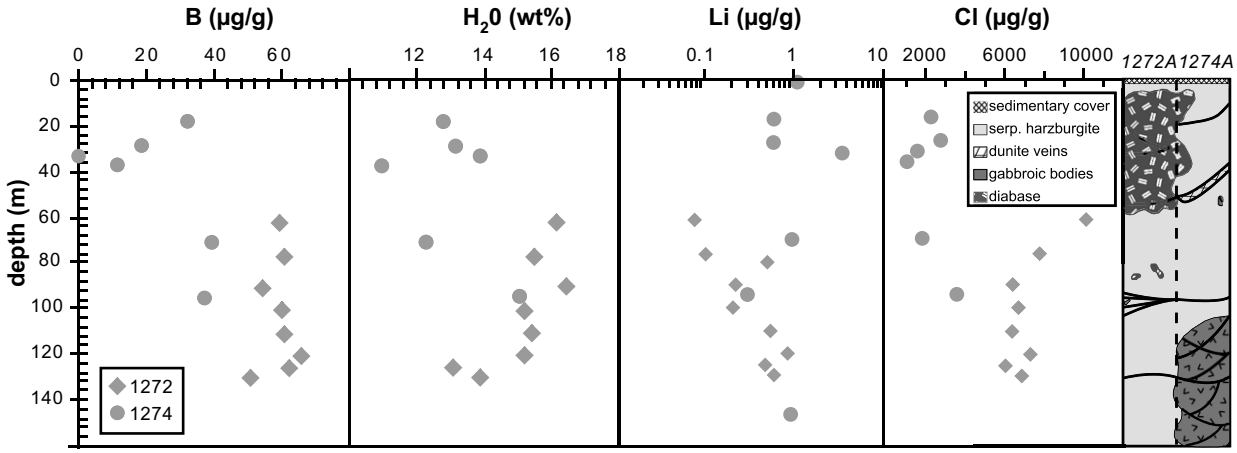

Fig. 8. Down hole distribution of B, Li, H_2O, Cl contents of whole rock analyzes and a simplified stratigraphic log (modified after Bach et al., 2004). Black lines in the log: deformation zones. ODP Leg 209 Site 1272A (grey diamonds) and Site 1274A (grey dots). B, H_2O and Cl data are listed in Table 5, Li data from isotope dilution (Vils et al., 2008).

ODP Leg 209 is among the most depleted of all abyssal peridotites, indicating partial melting exceeding 20% (Fig. 7a; see also Godard et al., 2008). A similar conclusion can be drawn on the degree of partial melting when considering the relation between Mg# of olivine and Cr# of spinel (Fig. 7b). Based on mineral compositions from Site 1274A, Seyler et al. (2007) explain this high degree of depletion with a two-stage partial melting/melt–rock reaction history, with an early melting in the garnet stability field.

In the studied samples, there is little textural, but widespread chemical evidence that the peridotite at both studied sites was infiltrated by mafic melts prior to serpentinization. Interstitial clinopyroxene forms textures with primary minerals (now pseudomorphosed by serpentine; Fig. 3a) that strongly resemble textures of melt pockets and primary minerals obtained with mantle rocks during deformation experiments (e.g. Bussod and Christie, 1991; Kohlstedt and Zimmerman, 1996; de Kloe et al., 2000). Seyler et al. (2001, 2007) interpreted similar clinopyroxene as left over from an interstitial melt. We thus interpret the interstitial clinopyroxene as crystallized from a melt, as described for ophiolites (e.g. Dijkstra et al., 2001; Müntener and Piccardo, 2003; Müntener et al., 2004).

Most of the clinopyroxene grains measured in this study show no TiO_2 enrichment and plot within the abyssal peridotites field (Fig. 6). In contrast, sample OD 42 shows a trend towards melt enrichment, while the samples OD 38 and OD 48 show pronounced signatures of TiO_2 enrichment. The major element compositions of clinopyroxene obtained in this study (Figs. 4–7) are consistent with the earlier microprobe data from ODP Leg 209 Site 1274A (Seyler et al., 2007; Moll et al., 2007).

The B and Li contents of interstitial clinopyroxene are in line with the hypothesis that these grains crystallized from an infiltrating melt. Compared to normal mantle clinopyroxene, interstitial clinopyroxene is variably enriched in B

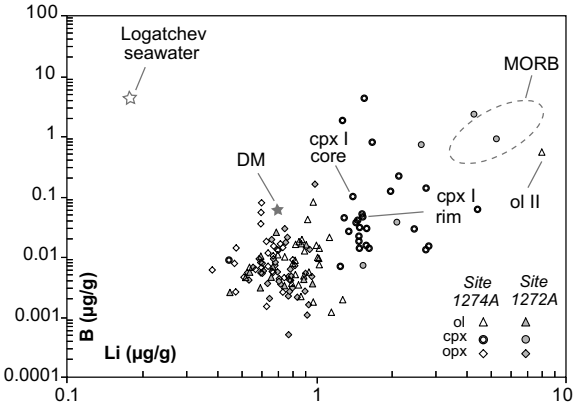

Fig. 9. Light element data obtained by SIMS analysis of primary minerals from ODP Leg 209 Sites 1272A and 1274A. Cpx I, primary cpx (OD 32); ol II, magmatic olivine. (OD42), Depleted mantle value after Salters and Stracke (2004), errors on these values are 8% for Li and 91% for B. Seawater value after Schmidt et al. (2007), MORB-field after Ryan and Langmuir (1987); Ryan and Langmuir (1993).

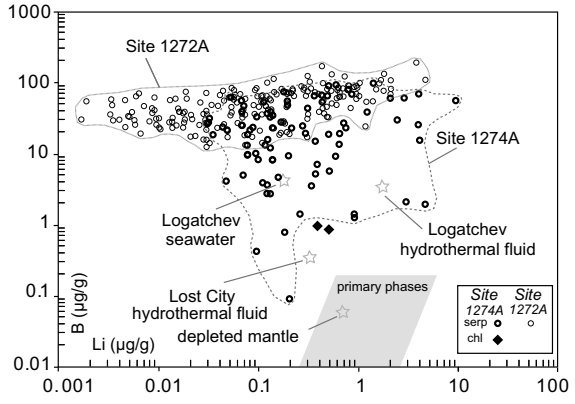

Fig. 10. Light element data of serpentine minerals obtained by SIMS-analysis of secondary minerals from ODP Leg 209 Site 1272A and 1274A. Depleted mantle value after Salters and Stracke (2004). Seawater and hydrothermal fluid value after Schmidt et al. (2007), Lost City data (Boschi, 2006).

and Li, with a trend towards the MORB field (Fig. 9). According to Seitz and Woodland (2000), Li enrichment in clinopyroxene compared to olivine and orthopyroxene can be related to metasomatism by mafic silicate melts or hydrous fluids. The preferential incorporation of Li in clinopyroxene during impregnation of peridotite by mafic melt was also reported by Eggins et al. (1998), McDade et al. (2003), Ottolini et al. (2004), Woodland et al. (2004) and Pelletier (2008).

An alternative explanation for the preferential enrichment of Li would be fractionation upon cooling. Coogan et al. (2005) performed experiments on Li diffusion in clinopyroxene at 800–1000 °C and observed that Li diffused into clinopyroxene within hours. Jeffcoate et al. (2007) also suggested higher diffusivity of Li in clinopyroxene compared to olivine for phenocrysts from Hawaiian basalts. In the studied samples, however, we observe that olivine and orthopyroxene show Li abundances typical of minerals from the depleted mantle (Fig. 9), while clinopyroxene is enriched in Li. Inter-mineral diffusive re-equilibration would have depleted olivine and orthopyroxene in Li. Also, the only primary clinopyroxene grain that could be analyzed shows no zoning in Li, which could support the hypothesis of fractionation upon cooling. We therefore conclude that the principal process controlling Li enrichment in clinopyroxene is melt infiltration.

6.3. The impact of serpentinization

As shown above, serpentinization had almost no impact on the composition of primary phases, but it modified the whole rock composition, in particular B contents, by formation of serpentine. Fig. 10 and Table 4 reveal that B contents of serpentine are much higher than those of primary minerals and than values for the depleted mantle. Most serpentine grains show B abundances between 10 and 100 μg g^{-1}. The variability of B abundances in serpentine is higher at Site 1274A (on average less serpentinized) than at Site 1272A (almost completely serpentinized), the latter showing generally higher absolute values (Fig. 10). There is no simple positive correlation between the degree of serpentinization and B whole rock contents (Fig. 8). However, the variability of B abundances in whole rock samples is higher at Site 1274A than at Site 1272A, the latter showing generally higher values (Fig. 11). A similar conclusion can be drawn from sulfur and from oxygen isotopes (Alt et al., 2007). At site 1274A, more primary sulfide minerals are preserved (e.g. pentlandite, chalcopyrite, bornite) and oxygen isotopic composition is within the range for depleted mantle (Alt et al., 2007). At site 1272A, primary sulfides are almost completely transformed to awaruite and heazlewoodite, testifying to desulfurization under reducing conditions due to serpentinization (Bach et al., 2004), and $\delta^{18}O$ values are enriched, pointing to more extensive interaction with seawater or a seawater-derived fluid than at site 1274A (Alt et al., 2007).

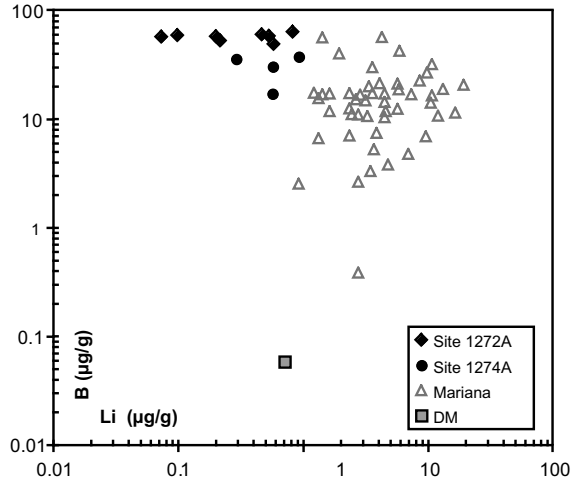

Fig. 11. Diagram showing measured Li and B contents of whole rock samples from the oceanic domain. Data for samples from Mariana forearc mud volcanoes (ODP Leg 215) are from Savov et al. (2005); the value for the depleted mantle (DM) is from Salters and Stracke (2004).

The positive correlation of B, Cl and H_2O implies that serpentinzation is the main process for B and Cl enrichment in ultramafic rocks. Cl contents correspond to average values for serpentinized mantle samples (Barnes and Sharp, 2006; Bonifacie et al., 2007), and show trends similar to H_2O.

Literature data confirm that serpentinization increases the B contents of oceanic mantle rocks (e.g. Bonatti et al., 1984; Thompson and Melson, 1970). Serpentinization at oceanic ridges is commonly triggered by heated seawater that cycles through the crust and parts of the lithospheric mantle and slowly alters the oceanic plate. As B is abundant in seawater (4.6 μg g^{-1}, Quinby-Hunt and Turekian, 1983; Jean-Baptise et al., 1991) compared to depleted mantle (0.04 μg g^{-1}, Table 6), seawater–peridotite interaction should enrich the mantle in B. Various studies on dredged abyssal peridotites have confirmed this enrichment in serpentinite (Thompson and Melson, 1970; Bonatti et al., 1984; Spivack and Edmond, 1987; Boschi et al., 2008), and studies on alpine serpentinite have demonstrated a large variability of B contents in serpentine (Scambelluri et al., 2004; Pelletier et al., 2008).

Experiments on chemical exchange between seawater and peridotite showed that at high temperature B is probably not incorporated into the rock but remains in solution (Seyfried and Dibble, 1980). However, during slow cooling below 300 °C, a B loss from the fluid was observed (partially driven by a change in pH). This implies that the major uptake of B by peridotites takes place at temperatures below 300 °C (Seyfried and Dibble, 1980).

The variation of B concentrations in the studied samples could also be due to changes in pH and temperature of the reacting fluid. For incorporating B in silicates, tetrahedrally coordinated boron, $B(OH)^{4-}$, is required (Spivack and Edmond, 1987). Palmer and Swihart (1996) demonstrated the pH dependency of $B(OH)^{4-}$ availability in fluids. Their results show that only at pH >8 significant concentrations of tetrahedrally coordinated boron complexes are present. At pH values lower than 6, $B(OH)^{4-}$ is absent in the fluid and B is not enriched in the minerals (Palmer and Swihart,

Table 6
Lithium and boron budget into subduction zone

	Sediment (clay)	MORB (altered)	MORB (fresh)	Gabbro	Peridotite (80% serp)	DM (harz)	
Density (kg m^{-3})	2700	2690	2900	2900	2530	3300	
Li (μg/g)	44.65	14.89	5.65	1	0.62	0.8	
B (μg/g)	83.91	40	1.99	2.7	40.92	0.04	
Data source	1	4 and 5	2 and 3	6 and 7	This study	This study	
1 m^3 contains							
Total Li (g)	120.56	16.39	40.05	2.90	2.05*	2.64	
Total B (g)	226.56	5.77	107.60	7.83	135.04*	0.13	
Semail-type lithosphere							Total
1-Ma-old plate					Total serp*		(t/col)
Thickness (km)	0	0.2	1.8	3.6	0		
% Li	–	16.71	61.52	21.78	–		0.048
% B	–	35.81	17.29	46.91	–		0.060
75-Ma-old plate							
Thickness (km)	0.3	1.5	0.5	3.6	20	54.1	
% Li	11.80	19.60	2.67	3.41	15.95	46.58	0.307
% B	7.52	17.85	0.32	3.12	70.66	0.79	0.904
ODP Leg 209-typ lithosphere							
1-Ma-old plate							
Thickness (km)	0	0.06	0	0.01	0.13	5.4	
% Li	–	14.17	–	0.17	1.57	84.09	0.017
% B	–	26.03	–	0.32	70.78	2.87	0.025
75-Ma-old plate							
Thickness (km)	0.3	0.06	0	0.01	20	59.63	
% Li	14.77	0.98	–	0.01	19.96	64.28	0.245
% B	9.45	0.90	–	0.01	88.86	1.09	0.719
DM (harzburgite)							
	Ol	Cpx	Opx	Spl	Total		
% Modal	66	3	30	1	100		
Li (μg/g)	0.80	2.04	0.69	0.51	0.80		
B (μg/g)	0.011	1.035	0.012	0.008	0.042		

Unit thickness see Fig. 14; DM (depleted mantle) calculation based on mineral average content from ODP leg 209. *first 3 km 80% serpentinization, rest 20% serpentinization used in the model (Li = 2.39 g and B = 27.11 g); col, column with x km depth and 1 m^2 surface; Li and B content are average data after: (1) Ishikawa and Nakamura (1993); (2) Ryan and Langmuir (1987); (3) Ryan and Langmuir (1993); (4) Bouman et al. (2004); (5) Thompson and Melson (1970); (6) Chan et al. (2002); (7) Smith et al. (1995).

1996). Bonatti et al. (1984) showed a negative correlation between temperature and B concentration in abyssal peridotites from the Vema and Romanche Fracture zones, using O^{18}/O^{16} fractionation between coexisting magnetite and serpentine as a thermometer (Wenner and Taylor, 1971). This simple relationship has been questioned by Plas (1997). His results from abyssal peridotites of different MOR (ODP Leg 107, 147, 149) for B and $\delta^{18}O$ showed that there is no simple correlation between temperature, serpentine mineral type and B content (Plas, 1997). For Lost City, Boschi et al. (2008) report B incorporation into serpentine at moderate temperatures, with random B—$\delta^{18}O$ distribution, supporting the hypothesis of Plas (1997).

The Li contents of serpentine in the studied samples range from 0.001 to 9.38 μg g^{-1}. The high abundances may in part be due to analyses of mixtures of serpentine with primary (cpx, opx, and ol) or secondary phases (brucite and iowaite). If the latter show the same light element characteristics as clay minerals they should be rich in Li. In any case, the Li contents of serpentine from Sites 1272A and 1274A are on the average lower than those of primary minerals (Fig. 10). Serpentinization, on average, should thus decrease Li contents of the whole rock samples. Serpentine from Site 1274A (less serpentinized) shows a smaller variation in Li contents and tends to higher values compared to serpentine from Site 1272A (almost completely serpentinized), which shows a larger variation and tends to lower values (Fig. 10).

The Li whole rock contents range from 0.72 to 1.04 μg g^{-1} (Vils et al., 2008) and are within the range measured by Paulick et al. (2006) and Godard et al. (2008; 0.04–1.37μg g^{-1}). They are, on average, lower than values for the depleted mantle (Fig. 11). Samples from the less serpentinized Site 1274A tend to higher and more uniform values than samples from Site 1272A, which show a larger variation and a lower average of Li contents (Fig. 11). As for B, there is no simple linear correlation between the degree of serpentinization and Li whole rock contents. On the other hand, Fig. 11 shows a significant difference between Mariana forearc samples (ODP Leg 125) and ODP Leg 209. Pore water measurements at the Mariana forearc showed high B (0.96–42.9 μg g^{-1}) and low Li abundance in the fluids (0.0001–0.07 μg g^{-1}; Mottl et al., 2004), the latter being probably the source of the enriched B and Li con-

centrations of the Mariana samples with respect to the ODP Leg 209 samples.

Less is known about the incorporation of Li into serpentine and serpentinite than for B. Whole rock studies on dredged abyssal peridotites have shown a considerable enrichment of serpentinized peridotite in Li compared to depleted mantle values, but with large variations (0.6–13.4 μg g^{-1}; Decitre et al., 2002; Niu, 2004). In-situ analysis of serpentine for Li revealed even larger variability (Decitre et al., 2002). In analogy to the results of heating experiments conducted on altered basalt (Seyfried et al., 1998), it may be concluded that Li incorporation in serpentine is favored at temperatures below 350 °C.

In summary, the systematics of B and Li observed in serpentine and serpentinite from Sites 1272A and 1274A suggest that the B and Li budget is strongly controlled by the degree of serpentinization, although there are large variations on the sample and the thin section scale. This suggests that the light element budget should depend strongly on water/rock ratios. In their study on serpentinized peridotite from Lost City, Boschi et al. (2008) observed that B content and $\delta^{11}B$ values show a strong positive correlation with water/rock ratios, the latter calculated by using the Sr isotopic composition of the rocks. For ODP Leg 209, we measured high $\delta^{11}B$ and high B content and calculated high water/rock ratios using the Sr isotopic composition of the serpentinites (Vils et al., 2008).

The potential role of temperature and pH is difficult to assess, because there are no direct indications from the two sites. Concerning temperature, we assume that within each of the two sites any temperature gradient must have been negligible given that the rocks cover a vertical distance of only 147 m (Table 1). There may have been a systematic temperature difference between the two sites given the large horizontal distance (Fig. 1), but Alt et al. (2007) derive serpentinization temperatures $\leqslant$150 °C at both sites on the basis of oxygen isotope data of serpentinites and gabbros. In addition there seems to be a chemical difference between the two Sites (Fig. 4–7). Spinel compositions show a lower degree of partial melting at Site 1272A compared to Site 1274A.

Indications of temperature and pH during water-rock interaction on the ocean floor come from two hydrothermal fields at the MAR, Logatchev and Lost City. The Logatchev hydrothermal field lies approximately 50 km south of Site 1272A. Fluids emerging from this site have temperatures of 353 °C and a pH of 3.3 (Douville et al., 2002 and Schmidt et al., 2007). They contain 3.63 μg g^{-1} B and 1.75 μg g^{-1} Li and are interpreted as chemically buffered by ultramafic and mafic rocks (Schmidt et al., 2007). The Li content in fluids buffered by only mafic rocks should be generally higher than for ultramafic systems (e.g. Snakepit 5.85 μg g^{-1} Li, Douville et al., 2002), but may be difficult to predict for mixed systems. At the Logatchev hydrothermal field, serpentinization enriched the reacting seawater in Li and depleted it in B. The ODP Leg 209 mineral and whole rock B and Li data are in line with such a process, although the fluids from Logatchev contain too much B to be in equilibrium with peridotites only from sites 1272A and 1274A. However, this difference may be explained by the fact that we studied an (almost) pure ultramafic system, while the Logatchev fluids represent a mafic-ultramafic system.

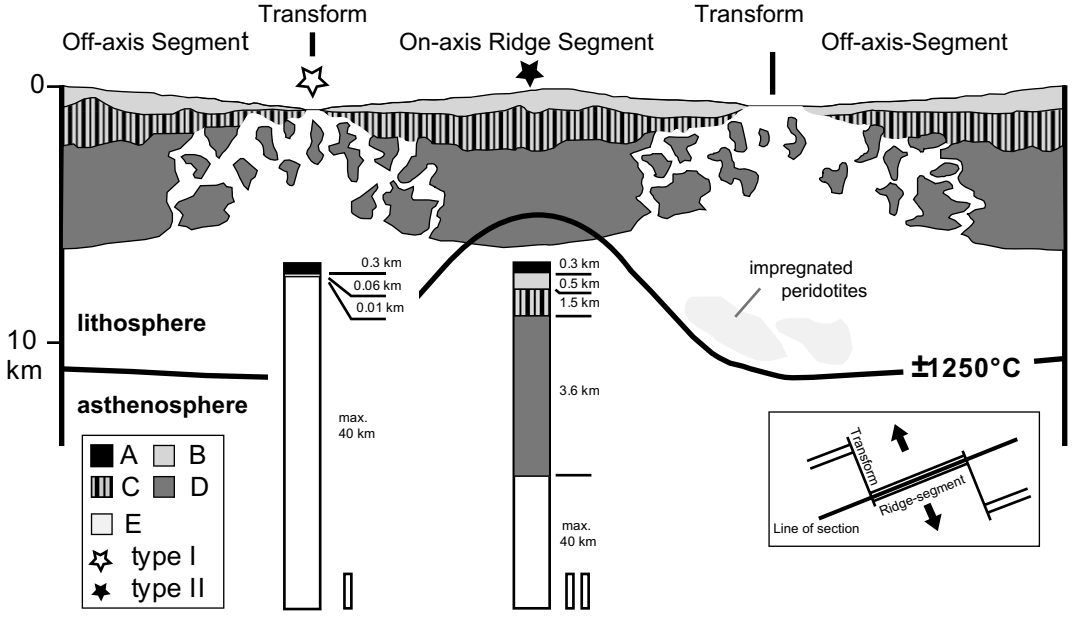

Fig. 12. Cross section through a mid-ocean ridge (modified after Ghose et al., 1996; Dijkstra et al., 2001). Type I: modified cross-section through ODP 209-type lithosphere after 75 Ma (modified after Bach et al., 2004). Type II: simplified cross-section through a Semail-type lithosphere after 75 Ma (modified after Boudier and Nicolas, 1985). (A) Sedimentary cover, (B) pillow basalts (completely altered), (C) sheeted dykes (fresh basalt), (D) gabbros, (E) plagioclase peridotites, white: mantle. Stars indicate possible location of type I and II on a mid-ocean ridge.

In 2000, an expedition discovered an off-axis hydrothermal field near the summit of the Atlantic massif: Lost City, a cold hydrothermal system driven by the exothermic serpentinization reaction (Kelley et al., 2001; Früh-Green et al., 2003; Kelley et al., 2005). From the white smokers a fluid with 40–75 °C and a pH of 9–9.8 emerges (Kelley et al., 2001). These hydrothermal fluids from Lost City are depleted in B and slightly enriched in Li compared to seawater (0.34 μg g^{-1} B and 0.33 μg g^{-1} Li; Boschi, 2006). Thus, also the data from this hydrothermal field show that the reacting fluid is enriched in Li and depleted in B after percolation through ultramafic rocks, although temperature and pH are very different from the Logatchev hydrothermal field. This suggests that these two parameters may be less important for the B and Li budget of the serpentinite samples from Sites 1272A and 1274A than the water/rock ratios.

6.4. Model of the B and Li budget of the oceanic lithosphere

The data presented in this study have shown that serpentinized oceanic mantle can be considerably enriched in B and slightly depleted in Li compared to depleted mantle values. B contents seem to increase with the degree of

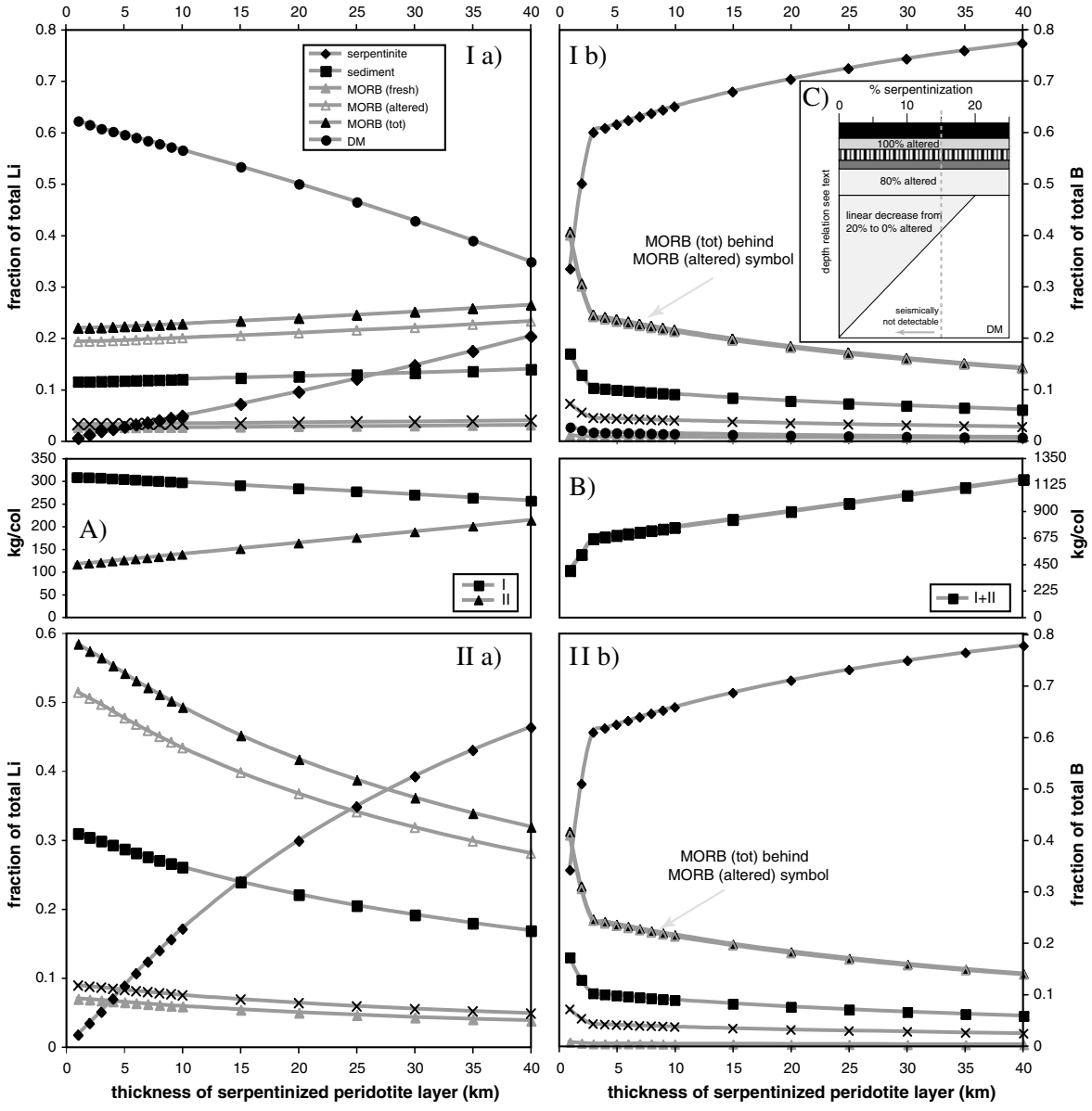

Fig. 13. Modeled evolution of the B and Li contents in a Semail-type lithosphere as a function of the thickness of the serpentinized layer, considering two cases: (I) the total thickness of the oceanic lithosphere is fixed to 80 km and (II) the total lithospheric thickness increases with age and serpentinization. (A and B) The total amount of Li and B content in a column of x km depth with 1 m^2 surface (x = thickness of the lithosphere). Input values are given in Table 6. (C) Simplified cross-section through an ocean plate, indicating degree of alteration/serpentinization with depth, as described in the text. Same symbols used as in Fig. 12 (figure not to scale).

serpentinization, while Li seems to show the opposite trend. This implies that serpentinization of oceanic mantle fractionates B from Li. This is opposite to what is found in igneous oceanic crust, where both B and Li are added by alteration processes (see Section 1).

Based on field and experimental data, Scambelluri et al. (2004) and Tenthorey and Hermann (2004) proposed that serpentinites are a major source of B into subduction zones. On the other hand, previous studies (see Section 1) have shown that—although volumetrically less important—the oceanic crust may also be an important reservoir of light elements. In addition, the proportions of igneous crust and mantle, the degree of hydrothermal alteration of the mantle, and the thickness of the lithosphere can vary considerably from one oceanic plate to another. Based on our results and on literature data, we model the budget of B and Li contained in the oceanic lithosphere, and its partitioning between crust and mantle as a function of plate characteristics. This represents an estimate of total B and Li potentially available in a subducting oceanic plate. We will first discuss the rationale and the parameters of our model. Then, we will present the results and discuss them against the background of published estimates of B and Li loss in subduction zones. Beryllium was not considered in our model because our data shows Be to be mostly around the critical value (<3 ng g^{-1}), independent of the degree of serpentinization. Also, the depleted mantle in general has very low Be contents (25 ng g^{-1}, Salters and Stracke, 2004). The Be content would be largely dominated by the sedimentary cover, because sediments can be

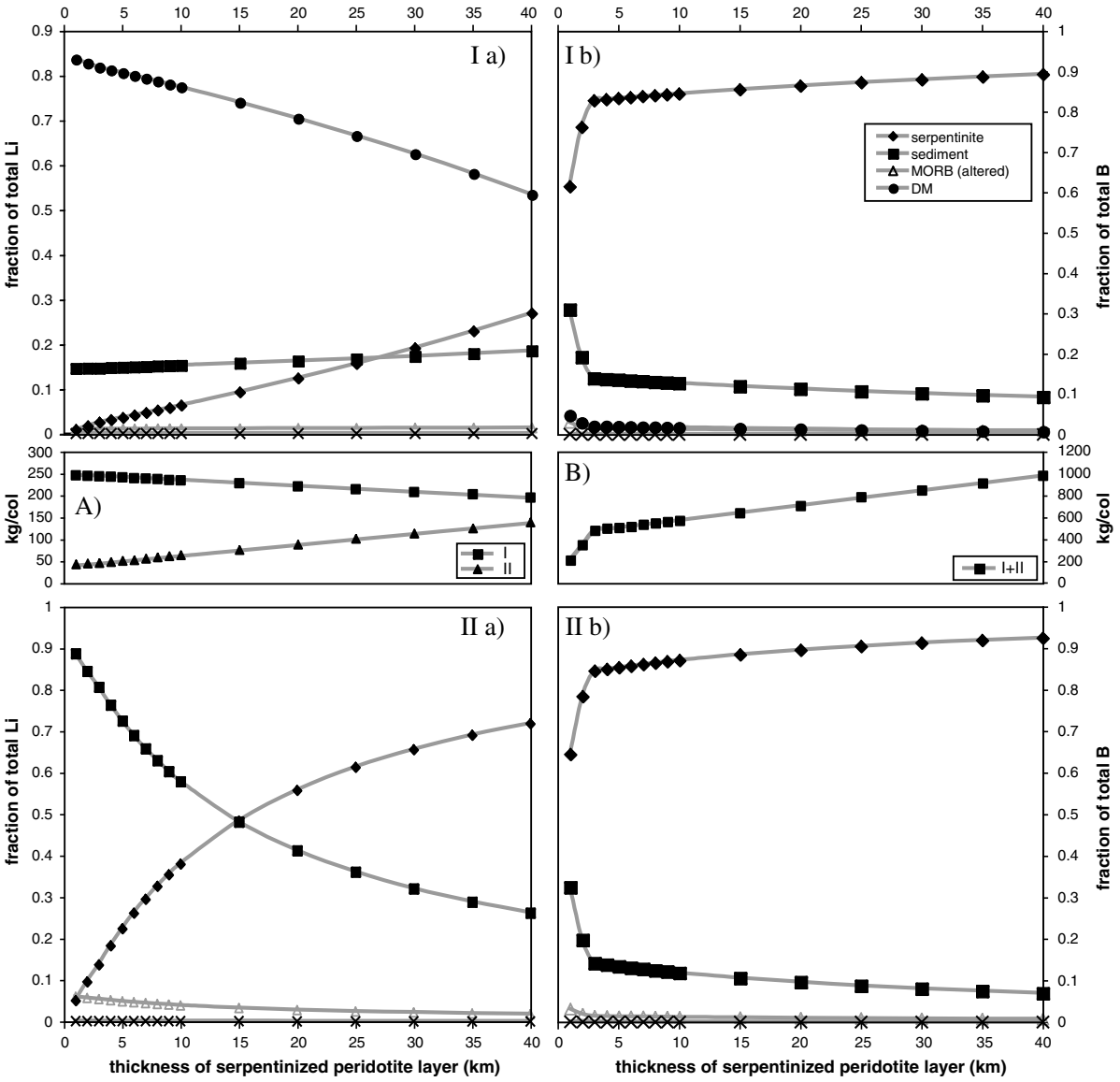

Fig. 14. Modeled evolution of the B and Li contents in a ODP Leg 209-type lithosphere as a function of the thickness of the serpentinized layer, considering two cases: (I) the total thickness of the oceanic lithosphere is fixed to 80 km and (II) the total lithospheric thickness increases with age and serpentinization. (A and B) The total amount of Li and B content in a column of x km depth with 1 m^2 surface (x = thickness of the lithosphere). Input values are given in Table 6.

enriched in Be up to the μg g^{-1}-level (e.g. Gao et al., 1998) and/or by the mafic crust (see compilation in Ryan, 2002).

6.5. Model parameters and rationale

Two parameters need to be considered when modeling the B and Li budget of the oceanic lithosphere. The first parameter is primary lithology. Geophysical data obtained in the oceanic domain (e.g. The MELT seismic team, 1998) and studies on ophiolites with largely coherent crust–mantle sections (Semail, Oman; Boudier and Nicolas, 1985) have shown that at fast-spreading ridges the igneous crust may be up to 7 km thick. On the other hand, at slow-spreading ridges such as the MAR, the igneous crust can be completely absent and the mantle exposed on the ocean floor (such as at Site 1274A, ODP Leg 209). Also, petrostructural studies on the Romanche and Vema fracture zones (Mid-Atlantic Ridge) have stressed the importance of oceanic fracture zones for locally exhuming serpentinized mantle to shallow depths, creating lithologically variable crust-mantle sections (Bonatti and Honnorez, 1976). As 'endmember' cases of oceanic lithosphere for our modeling we therefore use a lithospheric mantle with an igneous crust corresponding to that of the Semail ophiolite (Fig. 12, Table 6) and one with almost no igneous crust, such as that of to ODP Leg 209, Sites 1274A and 1272A (Fig. 12, Table 6). For both types of lithosphere, the published stratigraphic logs (Semail ophiolite: Boudier and Nicolas, 1985, ODP Leg 209: Bach et al., 2004) were simplified into six units: sediment, altered MORB, MORB, gabbro, serpentinized peridotite and depleted mantle (Fig. 12 and Table 6).

The second parameter, the age of the oceanic lithosphere, is important as it controls a considerable number of physical and chemical features. The total thickness of the oceanic lithosphere increases as the plate moves away from the ridge. In our model, we use plate ages of 1 and 75 Ma; the latter, because it corresponds to the average age of currently subducted oceanic plates (Li and Lee, 2006); the former because there are examples of very young oceanic lithosphere currently subducted, e.g. the Chile ridge (e.g. Tebbens et al., 1997), various oceanic basins in the western Pacific (e.g. Heaton and Hartzell, 1987), or about to be subducted (e.g. Macquarie Island, Sutherland, 1995; Lamarche et al., 1997).

Total lithospheric thickness as a function of age can be calculated with the GDH1 plate model of Stein and Stein (1992, 1996). According to this model, an oceanic plate has a total thickness of around 5 km after 1 Ma. In the case of a Semail-type lithosphere, this will correspond to the thickness of the igneous crust. In the case of an ODP Leg 209-type lithosphere, there will be 5 km of lithospheric mantle with minor volumes of igneous crust. After 75 Ma, both types of oceanic plates will have acquired a total thickness of approximately 80 km (Table 6).

The age of the lithosphere also controls the thickness of the sedimentary layer. To simplify modeling, we assume that any oceanic lithosphere will have no sedimentary cover at an age of 1 Ma and a 300-m sedimentary cover after 75 Ma (as is the case for the Semail ophiolite). We thus model in total four cases, an ODP Leg 209-type lithosphere, and a Semail-type lithosphere at 1 and 75 Ma, respectively (Table 6 and, Figs. 13 and 14).

The age of the lithosphere controls the vertical temperature gradient and hence the depth to which alteration by seawater-derived fluids plays a role/is possible. For the mantle part of the oceanic lithosphere it is important to note that the depth of serpentinization does not necessarily correspond to the depth of B enrichment/Li depletion. The major B incorporation in peridotites takes place at low temperatures (<300 °C, Seyfried and Dibble, 1980; Spivack and Edmond, 1987). In contrast, experiments showed that serpentine can be stable up to 650 °C at 3 GPa and up to 475 °C at 1 atm (Ulmer and Trommsdorff, 1995; Ulmer and Trommsdorff, 1999). For our model, we arbitrarily fixed the temperature limit of B enrichment/Li depletion at 300 °C and that of serpentinization at 550 °C and calculated the depth of both isotherms in the four endmember cases (Table 6) using the model of Parker and Oldenburg (1973) and Stein and Stein (1996). For the sake of simplicity, we assume the 300 °C also represents the limit of alteration in the igneous oceanic crust with respect to B and Li.

It is important to know to which degree the mantle at temperatures below the 300 °C isotherm is serpentinized. Experiments on water flow through partially serpentinized peridotite showed that serpentinization rates vary between 10^{-8} cm^2 s^{-1} at 34 °C to 10^{-4} cm^2 s^{-1} at 300 °C (MacDonald and Fyfe, 1985), indicating that in 1 Ma, 1 km of serpentinite layer can form at 300 °C, 260 m at 200 °C, and 60 m at 100 °C. These results indicate that serpentinization is a rather efficient process. It could be argued, however, that serpentine formation is also controlled by water availability and that this limit could be at shallower depth than the 300 °C isotherm. Although the oceans represent a virtually infinite reservoir, water can only penetrate the oceanic lithosphere through fractures or by diffusion. To our knowledge, there are no quantitative data on the penetration depth of water and the degree of serpentinization in off-ridge settings. However, MacDonald and Fyfe (1985) have shown that serpentinization proceeds by an efficient interplay of water diffusion and crack propagation due to volume increase during serpentinization. We therefore assume in our model that the mantle at temperatures below the 300 °C isotherm is serpentinized. The degree of serpentinization is difficult to assess. Escartin et al. (2001) showed that serpentinization degrees of 35% to 55% are necessary to obtain the reduced P-wave velocities of 6.5–7.5 km/s commonly observed in the oceanic lithosphere between normal crust and normal mantle. This layer has often been interpreted as serpentinized peridotite (e.g. Minshull et al., 1998). A wide-angle seismic experiment at the Atlantis II Fracture Zone, Southwest Indian Ridge (Muller et al., 1997) shows that a 3- to 4-km-thick igneous crust is underlain by a 2- to 3-km-thick layer of serpentinized mantle peridotite. The P-wave velocity of 6.9 km/s for the serpentinized peridotite layer corresponds to a 35 ± 10 vol % serpentine content (Escartin et al., 2001). A compilation of velocity structures of the oceanic crust/mantle in various tectonic settings (Minshull et al., 1998) shows that P-wave velocity of around 7 km/s, that can eventually be attributed to serpentinized mantle, are found between 1 and 6 km depth.

Taking all these lines of evidence into consideration, we fix the degree of serpentinization in our model to 80% (average degree observed in our samples: Tables 1 and 6) to a depth of 3 km. Below follows a much thicker layer where serpentinization decreases linearly from 20% to 0% (Fig. 13). Various test calculations, varying the thickness of the top layer between 1 and 3 km, have shown no significant difference.

B and Li input values for the mass balance are reported in Table 6. For the B and Li contents of the sedimentary layer, the data of Ishikawa and Nakamura (1993) were used, assuming the sediment to be composed only of clay minerals, known to incorporate high amounts of Li and B (Wunder et al., 2005; Wunder et al., 2006).

6.6. Results of mass balance calculations

The Li and B budgets are given in kilogram per column (kg/col). 1 column corresponds to 1 m × 1 m at the surface × the thickness of the lithosphere. As the thickness of the oceanic lithosphere varies with age, indicating kg/m^3 would not be useful. For case 1 (Semail-type lithosphere at an age of 1 Ma), the lithosphere is 5.6 km thick (total thickness of igneous crust in the Semail ophiolite), the 300 and 550 °C isotherms are located at 0.2 and 0.4 km depth, respectively (Table 6). The section is made up entirely of igneous crust (0.2 km of altered MORB, 1.8 km of MORB, 3.6 km of gabbro). At these conditions, the oceanic lithosphere contains on the average 48 kg/col Li and 60 kg/col B. Li is essentially hosted by MORB (61.5%). The major carriers of B are altered MORB (35.8%) and gabbro (46.9%). After 75 Ma, the 300 and 550 °C isotherms are located at 20 and 34 km depth, respectively. The section comprises from top to bottom: 0.3 km of sediment, 1.5 km of altered MORB, 0.5 km of MORB, 3.6 km of gabbro, 20 km of serpentinized peridotite enriched in B/depleted in Li, and 54.1 km of depleted mantle (Table 6). In this situation, the oceanic lithosphere contains on the average 307 kg/col Li and 904 kg/col B. Li resides mainly within the depleted mantle. It is hosted to a lesser degree by altered MORB (19.6%), serpentinized peridotites (16.0%) and sediment (11.8%). B is almost entirely hosted by serpentinized peridotite (70.8%).

For case 3 (ODP Leg 209-type lithosphere at an age of 1 Ma), the total lithospheric thickness is 5.6 km, the 300 and 550° isotherms are located at 0.2 and 0.4 km depth, respectively. At these conditions, the section comprises from top to bottom: 0.06 km of altered MORB, 0.01 km of gabbro, 0.13 km of serpentinized peridotite enriched in B/depleted in Li, and 5.4 km of depleted mantle (Table 6). In this situation, the oceanic lithosphere contains on the average 17 kg/col Li and 25 kg/col B. Table 6 shows that the Li budget of a slow spreading ridge will be predominantly hosted by the depleted mantle (84.1%), whereas B resides in serpentinized peridotite (70.8%) and in altered MORB (26.0%). After 75 Ma (case 4), the 300 and 550 °C isotherms will be located at 20 and 34 km depth, respectively. The oceanic lithosphere will have the same thickness of the igneous crust as at 1 Ma (0.06 km of altered MORB, 0.01 km of gabbro), but 0.30 km of sediment will have accumulated on top. Serpentinized peridotite will have increased to 20 km and depleted mantle to 59.63 km thickness. At these conditions, the oceanic lithosphere contains on average 245 kg/col Li and 719 kg/col B. The Li budget is dominated by the depleted mantle (64.3%), serpentinized peridotite (20.0%) and less by the sedimentary cover (14.8%). The B budget is largely controlled by serpentinized peridotite (88.9%). The (igneous) crust plays virtually no role for the Li and B budget in the ODP Leg 209-case.

6.7. Temporal evolution of the B and Li budget within the upper 40 km of the oceanic lithosphere—implications for subduction zones

From the mass balance calculations presented in the previous section, it is apparent that with increasing age of the lithosphere, the role of the depleted mantle as a reservoir for B and Li becomes increasingly important. In the context of B and Li recycling at subduction zones it can be argued that not the entire mantle volume dehydrates and liberates B and Li. For this setting, it may be more appropriate to consider only the B and Li budget of the upper part of the oceanic lithosphere (the 'dehydratable' part).

Moreover, there is evidence that additional serpentinization occurs due to fracturing during plate bending (e.g. Ranero et al., 2003; Ranero and Sallarès, 2004; Li and Lee, 2006), and may proceed to depth greater than 20 km (depth of the 300 °C isotherm in a 75-Ma-old plate) because of lower geothermal gradients and better water availability. By modeling seismic velocities of bending-related extensional faulting, Ranero and Sallarès (2004) predict a 20-km-thick mantle layer serpentinized to 17% for the Nazca plate at the North Chile trench. Based on geochemical data and modeling, Li and Lee (2006) estimate the paleo-serpentinization depth of the Feather River Ophiolite (subduction context) to be around 40 km.

In order to better account for this geodynamic context, we modeled the evolution of the B and Li budget only in the upper 40 km of the oceanic lithosphere, using the same input parameters as for our previous model, and applying it to two 'endmembers': a Semail-type lithosphere (Fig. 13) and an ODP Leg 209-type lithosphere (Fig. 14). In model cases I (Figs. 13Ia, b and 14Ia, b) we assume that the oceanic lithosphere has a constant thickness of 80 km, with the mantle part becoming increasingly serpentinized at conditions below 300 °C. This implies that initially, there are almost 80 km of depleted mantle, which are successively replaced by peridotite serpentinized at temperatures below 300 °C. In model cases II (Figs. 13IIa, b, and 14IIa, b) we assume that the lithospheric thickness increases by adding peridotite serpentinized at temperatures below 300 °C. This implies that there is no depleted mantle.

For boron, running the two models for the two endmembers provides similar results in all cases (Figs. 13Ib, IIb and 14Ib, IIb). Independent of the lithology of the oceanic plate, the B budget will be almost entirely controlled by serpentinized peridotite. Even in Semail-type lithosphere with a 5.6-km-thick igneous crust, a 3-km-thick section of serpentinized peridotite will be sufficient to host approxi-

mately 40% of the lithospheric B budget. These results suggest that large quantities of B reside in the uppermost part of the plate and could hence be easily liberated during slab dehydration.

For lithium, running the two models shows that the lithology of the oceanic plate controls the partitioning and availability of this element (Figs. 13Ia, IIa and 14Ia, IIa). In oceanic lithosphere containing a considerable fraction of depleted mantle (40%–50%), the Li budget is dominated by the latter (Figs. 13Ia and 14Ia). In oceanic lithosphere where depleted mantle is absent, Li is essentially hosted in sediments and in MORB (Figs. 13Ib and 14Ib). All of the figures related to Li show that serpentinized peridotite only becomes important for the Li budget once its thickness exceeds 20–25 km. These results suggest that the most prominent input of Li into subduction zones is to be expected from Semail-type lithosphere with a significant crustal section and a depleted mantle section, because in this situation most of the Li is stored at shallow levels in the plate. Subducting an ODP Leg 209-type lithosphere and assuming that most of the Li is liberated from the upper part of the plate would mean only very little Li output from the slab.

7. SUMMARY AND CONCLUSIONS

The results of our study of serpentinized peridotites from the Mid-Atlantic Ridge show that the B, Li and Be contents of the mantle minerals olivine, orthopyroxene and clinopyroxene remain unchanged during serpentinization and still reflect older processes such as melt infiltration. As serpentine has high B and fairly low Li contents, the process of serpentinization increases the B (and H_2O and Cl) and lowers the Li contents of the whole rock. These findings are in line with the composition of hydrothermal fluids sampled from the ocean floor, which are enriched in Li and depleted in B after percolation through ultramafic rocks.

The results of our mass balance calculations show that the Li contents of the oceanic lithosphere are highly variable and controlled by primary lithology whereas the B contents depend entirely on serpentinization. In all cases, large quantities of B reside in the uppermost part of the plate and could hence be easily liberated during slab dehydration. Late-stage serpentinization during slab bending will probably further increase the B content in the downgoing slab. The most prominent input of Li into subduction zones is to be expected from Semail-type lithosphere whereas subducting an ODP Leg 209-type lithosphere would be a far less efficient mechanism. Serpentinized mantle thus plays an important role in B recycling in subduction zones, but it is of lesser importance for Li.

ACKNOWLEDGMENTS

This research used samples provided by the Ocean Drilling Program (ODP). ODP is sponsored by the U.S. National Science Foundation (NSF) and participating countries under management of Joint Oceanographic Institutions (JOI), Inc.. Funding for this research was provided by the Swiss National Science Foundation (Grants 200021-10361 and 200021-103479/1). We thank E. Reusser (ETH Zürich, Switzerland), E. Gnos and A. Berger (Bern, Switzerland), H.-P. Meyer (Heidelberg, Germany) and H. Siegfried-Müller (Freiburg, Germany) for technical support at their microprobe and the PGAA team in Budapest for supplying B, H_2O and Cl whole rock data. Reviews by I. Savov, M. Godard and W. Bach helped to improve the manuscript.

REFERENCES

Alt J. C., Shanks, III, W. C., Bach W., Paulick H., Garrido C. J. and Beaudoin G. (2007) Hydrothermal alteration and microbial sulfate reduction in peridotite and gabbro exposed by detachment faulting at the Mid-Atlantic ridge, 15°20′N (ODP Leg 209): a sulfur and oxygen isotope study. *Geochem. Geophys. Geosyst.* **8**, 1–22.

Anders E. and Grevesse N. (1989) Abundance of the elements: meteoritic and solar. *Geochim. Cosmochim. Acta* **53**, 197–214.

Anderson D. L. and Kasztovszky Z. (2004) Application of PGAA with neutron beam. In *Handbook of Prompt Gamma Activation Analysis with Neutron Beams* (ed. G. L. Molnar). Kluwer, Dordrecht.

Arai S. (1994) Compositional variation of olivine–chromian spinel in Mg-rich magmas as a guide to their residual spinel peridotites. *J. Volcanol. Geotherm. Res.* **59**, 279–293.

Bach W., Garrido C. J., Paulick H., Harvey J. and Rosner M. (2004) Seawater–peridotite interactions: first insights from ODP Leg 209, MAR 15°N. *Geochem. Geophys. Geosyst.* **5**, 1–22.

Barnes J. D. and Sharp Z. D. (2006) A chlorine isotope study of DSDP/ODP serpentinized ultramafic rocks: insights into the serpentinization process. *Chem. Geol.* **228**, 246–265.

Benninghoven A., Rüdenauer F. G. and Werner H. W. (1987) *Secondary Ion Mass Spectrometry: Basic Concepts, Instrumental Aspects, Applications and Trends*. John Wiley and Sons, New York, Chichester, Brisbane, Toronto, Singapore.

Benton L. D., Ryan J. G. and Tera F. (2001) Boron isotope systematics of slab fluids as inferred from a serpentine seamount, Mariana forearc. *Earth Planet. Sci. Lett.* **187**, 273–282.

Benton L. D., Ryan J. G. and Savov I. P. (2004) Lithium abundance and isotopic systematics of forearc serpentinites, Conical Seamount, Mariana forearc: insights into the mechanics of slab–mantle exchange during subduction. *Geochem. Geophys. Geosyst.* **5**, 1–14.

Bonatti E. and Honnorez J. (1976) Section of the Earth's crust in the Equatorial Atlantic. *J. Geophys. Res.* **81**, 4104–4116.

Bonatti E., Lawrence J. and Morandi N. (1984) Serpentinization of oceanic peridotites: temperature dependence of mineralogy and boron content. *Earth Planet. Sci. Lett.* **70**, 88–94.

Bonifacie M., Busigny V., Mével C., Philippot P., Agrinier P., Jendrzejewski N., Scambelluri M. and Javoy M. (2007) Chlorine isotope composition in seafloor serpentinites and high-pressure metaperidotites. Insights into oceanic serpentinization and subduction processes. *Geochim. Cosmochim. Acta* **72**, 126–139.

Boschi C. (2006) *Building Lost City: Serpentinization, Mass Transfer and Fluid Flow in an Oceanic Core Complex*. Ph.D. Thesis, Swiss Federal Institute of Technology Zurich (ETH Zürich).

Boschi C., Früh-Green G., Delacour A., Karson J. A. and Kelley D. S. (2006) Mass transfer and fluid flow during detachment faulting and development of an oceanic core complex, Atlantis Massif (MAR 30°N). *Geochem. Geophys. Geosyst.* **7**, 1–39.

Boschi C., Dini A. and Fruh-Green G. L. (2008) Isotopic and element exchange during serpentinization and metasomatism at

the Atlantis Massif (MAR 30 degrees N): insights from B and Sr isotope data. *Geochim. Cosmochim. Acta* **72**, 1801–1823.

Boudier F. and Nicolas A. (1985) Harzburgite and lherzolite subtypes in ophiolitic and oceanic environment. *Earth Planet. Sci. Lett.* **76**, 81–92.

Bouman C., Elliott T. and Vroon P. Z. (2004) Lithium inputs to subduction zones. *Chem. Geol.* **212**, 59–79.

Brenan J. M., Neroda E., Lundstrom C. C., Shaw H. F., Ryerson G. F. J. and Phinney D. L. (1998) Behaviour of boron, beryllium and lithium during melting and crystallization: constraints from mineral–melt partitioning experiments. *Geochim. Cosmochim. Acta* **62**, 2129–2141.

Bussod G. Y. and Christie J. M. (1991) Textural development and melt topology in spinel lherzolite experimentally deformed at hypersolidus conditions. *J. Petrol.* **32**, 17–39.

Cannat M. (1993) Emplacement of mantle rocks in the seafloor at mid-ocean ridges. *J. Geophys. Res.* **98**, 4163–4172.

Chan L. H., Alt J. C. and Teagle D. A. H. (2002) Lithium and lithium isotope profiles through the upper oceanic crust: a study of seawater–basalt exchange at ODP Sites 504B and 896A. *Earth Planet. Sci. Lett.* **201**, 187–201.

Coogan L. A., Kasemann S. A. and Chakraborty S. (2005) Rates of hydrothermal cooling of new oceanic upper crust derived from lithium-geospeedometry. *Earth Planet. Sci. Lett.* **240**, 415–424.

Currie L. A. (1968) Limits for qualitative detection and quantitative determination. *Anal. Chem.* **40**, 586–593.

Decitre S., Deloule E., Reisberg L., James R., Agrinier P. and Mével C. (2002) Behavior of Li and its isotopes during serpentinization of oceanic peridotites. *Geochem. Geophys. Geosyst.* **3**. doi:10.1029/2001GC000178.

de Kloe R., Drury M. R. and van Roermund H. L. M. (2000) Evidence for stable grain boundary melt films in experimentally deformed olivine–orthopyroxene rocks. *Phys. Chem. Minerals* **27**, 480–494.

Dick H. J. B. and Bullen T. (1984) Chromian spinel as a petrogenetic indicator in abyssal and alpine-type peridotites and spatially associated lavas. *Contrib. Mineral. Petrol.* **86**, 54–76.

Dick H. J. B., Lin J. and Schouten H. (2003) An ultraslow-spreading class of ocean ridges. *Nature* **426**, 405–412.

Dijkstra A. H., Drury M. R. and Vissers R. L. M. (2001) Structural petrology of plagioclase peridotites in the West Othris Mountains (Greece): melt impregnation in mantle lithosphere. *J. Petrol.* **42**, 5–24.

Douville E., Charlou J. L., Oelkers E. H., Bienvenu P., Jove Colon C. F., Donval J. P., Fouquet Y., Prieur D. and Appriou P. (2002) The rainbow vent fluids (36°14′N, MAR): the influence of ultramafic rocks and phase separation on trace metal content in mid-atlantic ridge hydrothermal fluids. *Chem. Geol.* **184**, 37–48.

Eggins S. M., Rudnick R. L. and McDonough W. F. (1998) The composition of peridotites and their minerals: a laser-ablation ICP-MS study. *Earth Planet. Sci. Lett.* **154**, 53–71.

Elliott T., Thomas A., Jeffcoate A. and Niu Y. (2006) Lithium isotope evidence for subduction-enriched mantle in the source of mid-ocean-ridge basalts. *Nature* **443**, 565–568.

Escartin J. and Cannat M. (1999) Ultramafic exposures and the gravity signature of the lithosphere near the Fifteen–Twenty Fracture Zone (Mid-Atlantic Ridge, 14°–16.5 °N). *Earth Planet. Sci. Lett.* **171**, 411–424.

Escartin J., Hirth G. and Evans B. (2001) Strength of slightly serpentinized peridotites: implications for the tectonics of the oceanic lithosphere. *Geology* **29**, 1023–1026.

Escartin J., Mével C., MacLeod C. J. and McCaig A. M. (2003) Constraints on deformation conditions and the origin of oceanic detachments: the mid-atlantic ridge core complex at 15°45′N. *Geochem. Geophys. Geosyst.* **4**, 1–37.

Früh-Green G., Kelley D. S., Bernasconi S. M., Karson J. A., Ludwig K. A., Butterfield D. A., Boschi C. and Proskurowski G. (2003) 30,000 years of hydrothermal activity at the Lost City vent field. *Science* **301**, 495–498.

Fujiwara T., Lin J., Matsumoto T., Kelemen P. B., Tucholke B. E. and Casey J. F. (2003) Crustal evolution of the mid-atlantic ridge near the Fifteen–Twenty Fracture zone in the last 5 Ma. *Geochem. Geophys. Geosyst.* **4**, 1–25.

Gao S., Luo T.-C., Zhang B.-R., Zhang H.-F., Han Y.-W., Zhao Z.-D. and Hu Y.-K. (1998) Chemical composition of the continental crust as revealed by studies in East China. *Geochim. Cosmochim. Acta* **62**, 1959–1975.

Ghose I., Cannat M. and Seyler M. (1996) Transform fault effect on mantle melting in the MARK area (mid-atlantic ridge south of the Kane transform). *Geology* **24**, 1139–1142.

Gméling K., Harangi S. and Kasztovszky Z. (2005) Boron and chlorine concentrations of volcanic rocks: an application of prompt gamma activation analysis. *J. Radioanal. Nucl. Chem.* **265**, 204–214.

Godard M., Lagabrielle Y., Alard O. and Harvey J. (2008) Geochemistry of the highly depleted peridotites drilled at ODP Sites 1272 and 1274 (Fiffteen-Twenty Fracture Zone, Mid-Atlantic Ridge): implications for mantle dynamics beneath a slow spreading ridge. *Earth Planet. Sci. Lett.* **267**, 410–425.

Hamlyn P. R. and Bonatti E. (1980) Petrology of mantle-derived ultramafics from the Owen fracture zone, northwest Indian ocean: implications for the nature of the oceanic upper mantle. *Earth Planet. Sci. Lett.* **48**, 65–79.

Heaton T. H. and Hartzell S. H. (1987) Earthquake hazards on the Cascadia subduction zone. *Science* **236**, 162–168.

Hellebrand E., Snow J. E., Dick H. J. B. and Hofmann A. W. (2001) Coupled major and trace elements as indicators of the extent of melting in mid-ocean-ridge peridotites. *Nature* **410**, 677–681.

Hellebrand E., Snow J. E. and Mühe R. (2002) Mantle melting beneath Gakkel Ridge (Arctic Ocean). Abyssal peridotite spinel compositions. *Chem. Geol.* **182**, 227–235.

Ildefonse B., Blackman D. K., John B., Ohara Y., Miller D. J. and MacLeod C. J. (2007) Oceanic core complexes and crustal accretion at slow-spreading ridges. *Geology* **35**, 623–626.

Ishikawa T. and Nakamura E. (1993) Boron isotope systematics of marine sediments. *Earth Planet. Sci. Lett.* **117**, 567–580.

James R. H. and Palmer M. R. (2000) Marine geochemical cycle of the alkali elements and boron: the role of sediments. *Geochim. Cosmochim. Acta* **64**, 3111–3122.

Jean-Baptise P., Charlou J. L., Stievenard M., Donval J. P., Bougault H. and Mével C. (1991) Helium and methan measurements in hydrothermal fluids from the Mid-Atlantic ridge: the Sanke Pit Site at 23°N. *Earth Planet. Sci. Lett.* **106**, 17–28.

Jeffcoate A., Elliott T., Kasemann S. A., Ionov D., Cooper K. and Brooker R. A. (2007) Li isotope fractionation in peridotites and mafic melts. *Geochim. Cosmochim. Acta* **71**, 22–218.

Kelemen P. B., Kikawa E. and Miller D. J. (2004a) *Proceedings of the Ocean Drilling Program*. Preliminary Report Leg 209.

Kelemen P. B., Kikawa E. and Miller D. J. (2004b) *Proceedings of the Ocean Drilling Program*. Initial Reports 209.

Kelemen P. B., Kikawa E. and Miller D. J. (Eds.) (2007) *Proc. ODP, Sci. Results*. College Station, TX (Ocean Drilling Program), No. 209.

Kelley D. S., Karson J. A., Blackman D. K., Früh-Green G., Butterfield D. A., Lilley M. D., Olson E. J., Schrenk M. O., Roe K., Lebon G. T. and Rivizzigno P. (2001) An off-axis

hydrothermal field near the mid-atlantic ridge at 30°N. *Nature* **412**, 145–149.

Kelley D. S., Karson J. A., Früh-Green G., Yoerger D. R., Shank T. M., Butterfield D. A., Hayes J. M., Schrenk M. O., Olson E. J., Proskurowski G., Jakuba M., Bradley A., Larson B., Ludwig K., Glickson D., Buckman K., Bradley A. S., Brazelton W. J., Roe K., Elend M. J., Delacour A., Bernasconi S. M., Lilley M. D., Baross J. A., Summons R. E. and Sylva S. P. (2005) A serpentinite-hosted ecoystem: the Lost City hydrothermal field. *Science* **307**, 1428–1434.

Kisakürek B., Widdowson M. and James R. H. (2004) Behavior of Li isotopes during continental weathering: the Bidar laterite profile, India. *Chem. Geol.* **212**, 27–44.

Kohlstedt D. L. and Zimmerman M. E. (1996) Rheology of partially molten mantle rocks. *Annu. Rev. Earth Planet. Sci.* **24**, 41–62.

Kuhn et al. (2004) The hydrothermal field—revisited: preliminary results of the R/V Meteor cruise hydromar I (M60/3). *Interridge News* **13**, 1–4.

Lagabrielle Y., Bideau D., Cannat M., Karson J. A. and Mével C. (1998) Ultramafic-mafic plutonic rock suites exposed along the mid-Atlantic ridge (10°N–30°N). Symmetrical–asymmetrical distribution and implications for seafloor spreading processes. Faulting and magmatism at mid-ocean ridges. *Geophys. Monogr.* **106**, 153–176.

Lamarche G., Collot J.-Y., Wood R. A., Sosson M., Sutherland R. and Delteil J. (1997) The Oligocene–Miocene Pacific Australia plate boundary, south of New Zealand: evolution from ocean spreading to strike–slip faulting. *Earth Planet. Sci. Lett.* **148**, 129–139.

Leeman W. P., Tonarini S., Chan L. H. and Borg L. E. (2004) Boron and lithium isotopic variations in a hot subduction zone—the southern Washington Cascades. *Chem. Geol.* **212**, 101–124.

Li Z.-X. A. and Lee C.-T. A. (2006) Geochemical investigation of serpentinized oceanic lithospheric mantle in the Feather River Ophiolite, California: implications for the recycling rate of water by subduction. *Chem. Geol.* **235**, 161–185.

Lyubetskaya T. and Korenaga J. (2007) Chemical composition of Earth's primitive mantle and its variance. 1: Method and results. *J. Geophys. Res.*, 112.

MacDonald A. H. and Fyfe W. S. (1985) Rate of serpentinization in seafloor environments. *Tectonophysics* **116**, 123–135.

Marschall H. R. and Ludwig T. (2004) The low-boron contest. Minimising surface contamination and analysing boron concentration at the ng/g-level by secondary ion mass spectrometry. *Mineral. Petrol.* **81**, 265–278.

Marschall H., Kasztovszky Z., Gméling K. and Altherr R. (2005) Chemical analysis of high-pressure metamorphic rocks by PGNAA: comparison with results from XRF and solution ICP-MS. *J. Radioanal. Nucl. Chem.* **265**, 339–348.

Marschall H., Altherr R., Ludwig T., Kalt A., Gméling K. and Kasztovszky Z. (2006) Partitioning and budget of Li, Be and B in high-pressure metamorphic rocks. *Geochim. Cosmochim. Acta* **70**, 4750–4769.

McDade P., Blundy J. D. and Wood B. J. (2003) Trace element partitioning on the Tinaquillo Lherzolite solidus at 1.5 GPa. *Phys. Earth Planet. Interiors* **139**, 129–147.

McDonough W. F. and Sun S.-S. (1995) The composition of the Earth. *Chem. Geol.* **120**, 223–253.

Michael P. J., Langmuir C. H., Dick H. J. B., Snow J. E., Goldstein S. L., Graham D. W., Lehnert K., Kurras G., Jokat W., Mühe R. and Edmonds H. N. (2003) Magmatic and amagmatic seafloor generation at the ultraslow-spreading Gakkel ridge, Arctic Ocean. *Nature* **423**, 956–961.

Minshull T. A., Muller M. R., Robinson C. J., White R. S. and Bickle M. J. (1998) Is the oceanic Moho a serpentinization front? In *Modern Ocean Floor Processes and Geological Record*, 148 (eds. R. A. Mills and K. Harrison). Geological Society, London, pp. 71–80.

Moll M., Paulick H., Suhr G. and Bach W. (2007) Data report: microprobe analyses of primary phases (olivine, pyroxene, and spinel) and alteration products (serpentine, iowaite, talc, magnetite, and sulfides) in Holes 1268A, 1272A, and 1274A. In *Proc. ODP, Sci. Results* (eds. P. B. Kelemen, E. Kikawa and D. J. Miller), No. 209, pp. 1–13.

Molnar G. L. (2004) *Handbook of prompt gamma activation analysis with neutron beams*. Kluwer Academic Publishers, Dordrecht.

Mottl M. J., Wheat G. C., Fryer P., Gharib J. and Martin J. B. (2004) Chemistry of springs across the Mariana forearc shows progressive devolatilization of the subducting plate. *Geochim. Cosmochim. Acta* **68**, 4915–4933.

Muller M. R., Robinson C. J., Minshull T. A., White R. S. and Bickle M. J. (1997) Thin crust beneath ocean drilling program borehole 735B at the Southwest Indian Ridge? *Earth Planet. Sci. Lett.* **148**, 93–107.

Müntener, O. and Piccardo G. B. (2003) Melt migration in ophiolitic peridotites: the message from Alpine–Apennine peridotites and implications from embryonic ocean basins. In *Ophiolites in Earth History* (eds. Y. Dilek and P. T. Robinson). Geological Society of London, Special Publications 218, pp. 69–89.

Müntener O., Pettke T., Desmurs L., Meier M. and Schaltegger U. (2004) Refertilization of mantle peridotite in embryonic ocean basins: trace element and Nd-isotopic evidence and implications for crust–mantle relationships. *Earth Planet. Sci. Lett.* **221**, 293–308.

Niida K. (1997) Mineralogy of MARK peridotites: replacement through magma channeling examined from hole 920D, MARK area. *Proceedings of Ocean Drilling Program, Scientific Results* 153, pp. 265–275.

Niu Y. (2004) Bulk-rock major and trace element compositions of abyssal peridotites: implications for mantle melting, melt extraction and post-melting processes beneath mid-ocean ridges. *J. Petrol.* **45**, 2458–24223.

O'Hanley D. S. (1996) Serpentinites, records of tectonic and petrological history. *Oxford Monogr. Geol. Geophys.*, 34.

Ottolini L., Bottazzi P. and Vannucci R. (1993) Quantification of Lithium, Beryllium and Boron in silicates by secondary ion mass spectrometry using conventional energy filtering. *Anal. Chem.* **65**, 1960–1968.

Ottolini L., Le Fèvre B. and Vannucci R. (2004) Direct assessment of mantle boron and lithium contents and distribution by SIMS analyses of peridotite minerals. *Earth Planet. Sci. Lett.* **228**, 19–36.

Palmer M. R. and Swihart G. H. (1996) Boron Isotope Geochemistry: An Overview. *Rev. Mineral. Geochem.* **33**, 709–744.

Parker R. L. and Oldenburg D. W. (1973) Thermal model of ocean ridges. *Nat. Phys. Sci.* **242**, 137–139.

Parkinson I. J. and Pearce J. A. (1998) Peridotites from the Izu–Bonin–Mariana Forearc (ODP Leg 125): evidence for mantle melting and melt–mantle interaction in a supra-subduction zone setting. *J. Petrol.* **339**, 1577–1618.

Paulick H., Bach W., Godard M., De Hoog J. C. M., Suhr G. and Harvey J. (2006) Geochemistry of abyssal peridotites (Mid-Atlantic Ridges, 15°20′N, ODP Leg 209): implications for fluid/rock interaction in slow spreading environments. *Chem. Geol.* **234**, 179–210.

Pearce N., Perkins W. T., Westgate J. A., Gorton M. P., Jackson S. E., Neal C. R. and Chenery S. P. (1997) A compilation of new

and published major and trace element data for NIST SRM 610 and NIST SRM 612 glass reference materials. *Geostand. Newslett.* **21**, 115–144.

Pelletier L. (2008) *The Oceanic Mantle as an Important Repository for the Light Elements Li, Be and B*. Ph.D. thesis, University of Neuchâtel.

Pelletier L., Müntener O., Kalt A., Vennemann T.W. and Belgya T. (2008) Emplacement of ultramafic rocks into the continental crust monitored by light and other trace elements: an example from the Geisspfad body (Swiss–Italian Alps). *Chem. Geol.* **255**, 143–159. Available at: doi:10.1016/j.chemgeo.2008.06.024.

Pistiner J. S. and Henderson G. M. (2003) Lithium-isotope fractionation during continental weathering processes. *Earth Planet. Sci. Lett.* **214**, 327–339.

Plas A. (1997) *Petrologic and Stable Isotope Constraints on Fluid–rock Interaction, Serpentinization and Alteration of Oceanic Ultramafic Rocks*. Ph.D. Thesis, Swiss Federal Institute of Technology Zurich (ETH Zürich).

Prichard H. M. (1979) A petrographic study of the process of serpentinisation in ophiolites and the ocean crust. *Contrib. Mineral. Petrol.* **68**, 231–241.

Quinby-Hunt M. S. and Turekian K. K. (1983) Distribution of elements in sea water. *EOS* **64**, 130–132.

Ranero C. R. and Sallarès V. (2004) Geophysical evidence for hydration of the crust and mantle of the Nazca plate during bending at the north Chile trench. *Geology* **32**, 549–552.

Ranero C. R., Morgan P. J., McIntosh K. and Reichert C. (2003) Bending-related faulting and mantle serpentinization at the Middle America trench. *Nature* **45**, 367–373.

Révay Z., Molnar G. L., Belgya T., Kasztovszky Z. and Firestone R. B. (2001) A new gamma-ray spectrum catalog and library for PGAA. *J. Radioanal. Nucl. Chem.* **248**, 395–399.

Ross K. and Elthon D. (1997) Extreme incompatible trace-element depletion of diopside in residual mantle from south of the Kane fracture zone. In (eds. J. A. Karson, M. Cannat, D. J. Miller and Elthon, D. (Eds.), *Proceedings of the Ocean Drilling Program* 153, pp. 277–284.

Rudnick R. L., Tomascak P. B., Njo H. B. and Gardner R. l. (2004) Extreme lithium isotopic fractionation during continental weathering revealed in saprolites from South Carolina. *Chem. Geol.* **212**, 45–57.

Ryan J. G. (2002) Trace-element systematics of beryllium in terrestrial materials. In *Beryllium: Mineralogy, Petrology and Geochemistry* (eds. E. S. Grew, P. H. Ribbe and J. J. Rosso). Mineralogical Society of America, Washington DC.

Ryan J. G. and Langmuir C. H. (1987) The systematics of lithium abundances in young volcanic rock. *Geochim. Cosmochim. Acta* **51**, 1727–1741.

Ryan J. G. and Langmuir C. H. (1993) The systematics of boron abundances in young volcanic rocks. *Geochim. Cosmochim. Acta* **57**, 1489–1498.

Salters V. J. M. and Stracke A. (2004) Composition of the depleted mantle. *Geochem. Geophys. Geosyst.* **5**, 1–27.

Savov I. P., Ryan J. G., D'Antonio M., Kelley K. and Mattie P. (2005) Geochemistry of serpentinized peridotites from the Mariana Forearc Conical Seamount, ODP Leg 125: implications for the elemental recycling at subduction zones. *Geochem. Geophys. Geosyst.* **6**, 1–24.

Savov I. P., Ryan J. G., D'Antonio M. and Fryer P. (2007) Shallow slab fluid release across and along the Mariana arc-basin system: insights from geochemistry of serpentinized peridotites from the Mariana Forearc. *J. Geophys. Res.* **112**, B09205. doi:10.1029/2006JB004749.

Scambelluri M., Müntener O., Ottolini L., Pettke T. and Vannucci R. (2004) The fate of B, Cl and Li in the subducted oceanic mantle and in the antigorite breakdown fluids. *Earth Planet. Sci. Lett.* **222**, 217–234.

Schmidt K., Koschinsky A., Garbe-Schönberg D., de Carvalho L. M. and Seifert R. (2007) Geochemistry of hydrothermal fluids from the ultramafic-hosted hydrothermal field, 15 °N on the mid-atlantic ridge: temporal and spatial investigation. *Chem. Geol.* **242**, 1–21.

Scotese C. R., Gahagan L. M. and Larson R. L. (1988) Plate tectonic reconstructions of the Cretaceous and Cenozoic ocean basins. *Tectonophysics* **155**, 27–48.

Seitz H.-M. and Woodland A. B. (2000) The distribution of lithium in peridotitic and pyroxenitic mantle lithologies—an indicator of magmatic and metasomatic processes. *Chem. Geol.* **166**, 47–64.

Seyfried, Jr., W. E. and Dibble, Jr., W. E. (1980) Seawater–peridotite interaction at 300 °C and 500 bars: implications of the origin of oceanic serpentinites. *Geochim. Cosmochim. Acta* **44**, 309–321.

Seyfried, Jr., W. E., Chen X. and Chan L. H. (1998) Trace element mobility and lithium isotope exchange during hydrothermal alteration of seafloor weathered basalt: an experimental study at 350 °C, 500 bars. *Geochim. Cosmochim. Acta* **62**, 949–960.

Seyler M., Toplis M. J., Lorand J.-P., Luguet A. and Cannat M. (2001) Clinopyroxene microtextures reveal incompletely extracted melts in abyssal peridotites. *Geology* **29**, 155–158.

Seyler M., Lorand J.-P., Dick H. J. B. and Drouin M. (2007) Pervasive melt percolation reactions in ultra-depleted refractory harzburgites at the mid-atlantic ridge, 15°20′N: ODP Hole 1274A. *Contrib. Mineral. Petrol.* **153**, 303–319.

Sharapov V. N. and Simonov V. A. (1991) *Geologic investigations in the Central Atlantic*. Novosibirsk Institute of Geology and Geophysics, Siberian Branch of the USSR Academy of Science, 192 pp. (in Russian).

Shaw D. M., Higgins M. D., Truscott M. G. and Middleton T. A. (1988) Boron contamination in polished thin sections of meteorites: implications for the trace-elements studies by alpha-track image or ion microprobe. *Am. Mineral.* **73**, 894–900.

Shibata T. and Thompson G. (1986) Peridotites from the mid-atlantic ridge at 43°N and their petrogenetic relation to abyssal tholeiites. *Contrib. Mineral. Petrol.* **93**, 144–159.

Smith H. J., Spivack A. J., Staudigel H. and Hart S. R. (1995) The boron isotopic composition of altered oceanic crust. *Chem. Geol.* **126**, 119–135.

Spivack A. J. and Edmond J. (1987) Boron isotope exchange between seawater and oceanic crust. *Geochim. Cosmochim. Acta* **51**, 1033–1043.

Stein C. A. and Stein S. (1992) A model for the global variations in oceanic depth and heat flow with lithospheric age. *Nature* **359**, 123–129.

Stein S. and Stein C. A. (1996) Thermo-mechanical evolution of oceanic lithosphere: implications for the subduction process and deep earthquakes (overview). In *Subduction: Top to Bottom*, vol. 96 (eds. G. E. Bebout, D. W. Scholl, S. H. Kirby and J. P. Platt). AGU Geophysical Monograph, pp. 1–17.

Sudarikov S. M. and Roumiantsev A. B. (2000) Structure of hydrothermal plumes at the vent field, 14°45′N, mid-atlantic ridge: evidence from geochemical and geophysical data. *J. Volcanol. Geotherm. Res.* **101**, 245–252.

Sutherland R. (1995) The Australia-Pacific boundary and Cenozoic plate motions in the SW Pacific: some constraints from Geosat data. *Tectonics* **4**, 819–831.

Takahashi E., Uto K. and Schilling J. G. (1987) *Primary Magma Compositions and Mg/Fe Ratios of their Mantle Residues along Mid Atlantic Ridge 29°N to 73°N*. Technical Report ISEI, Okayama University Ser. A, pp. 1–14.

Taura H., Yurimoto H., Kurita K. and Sueno S. (1998) Pressure dependence on partition coefficients for trace elements between olivine and the coexisting melts. *Phys. Chem. Minerals* **25**, 469–484.

Tebbens S. F., Cande S. C., Kovacs L., Parra J. C., LaBrecque J. L. and Vergara H. (1997) The Chile ridge: a tectonic framework. *J. Geophys. Res.* **102**, 12035–12060.

Tenthorey E. and Hermann J. (2004) Composition of fluids during serpentinite breakdown in subduction zones: evidence for limited boron mobility. *Geology* **32**, 865–868.

The MELT Seismic Team (1998) Imaging the deep seismic structure beneath a mid-ocean ridge: the MELT experiment. *Science* 280, 1215–1218.

Thompson G. and Melson W. G. (1970) Boron contents of serpentinites and metabasalts in the oceanic crust: implications for the boron cycle in the oceans. *Earth Planet. Sci. Lett.* **8**, 61–65.

Tucholke B. E., Lin J. and Kleinrock M. C. (1998) Megamullions and mullion structure defining oceanic metamorphic core complexes on the mid-Atlantic ridge. *J. Geophys. Res.* **103**, 9857–9866.

Ulmer P. and Trommsdorff V. (1995) Serpentine stability to mantle depths and subduction-related magmatism. *Science* **268**, 858–861.

Ulmer P. and Trommsdorff V. (1999) Phase relations of hydrous mantle subducting to 300 km. In *Mantle Petrology: Field Observations and High Pressure Experimentation: A Tribute to Francis R. (Joe) Boyd* (eds. Y. Fei, C. M. Bertka and B. O. Mysen). The Geochemical Society, Special Publication No. 6, pp. 259–281.

Vils F., Tonarini S., Seitz H.-M., Kalt A. and Pelletier L. (2008) Are Li, B and Sr-isotopes tracers for serpentinization? *Geochim. Cosmochim. Acta* **72**, A985.

Viti C., Mellini M. and Rumori C. (2005) Exsolution and hydration of pyroxenes from partially serpentinized harzburgites. *Mineral. Mag.* **69**, 491–507.

Wei W., Kastner M., Dehyle A. and Spivack A. J. (2005) Geochemical cycling of fluorine, chlorine, bromine, boron and implications for fluid–rock reactions in Mariana forerc, South Chamorro Seamount, ODP Leg 195. In *Proceedings of Ocean Drilling Program, Scientific Results* **195**, pp. 1–23.

Wenner D. B. and Taylor H. P. J. (1971) Temperatures of serpentinization of ultramafic rocks based on O18/O16 fractionation between coexisting serpentine and magnetite. *Contrib. Mineral. Petrol.* **32**, 165–185.

Wicks F. J. and Whittaker E. J. W. (1977) Serpentine textures and serpentinization. *Can. Mineral.* **15**, 459–488.

Woodland A. B., Seitz H.-M. and Yaxley G. M. (2004) Varying behavior of Li in metasomatised spinel peridotite xenoliths from western Victoria, Australia. *Lithos* **75**, 55–66.

Wunder B., Meixner A., Romer R. L., Wirth R. and Heinrich W. (2005) The geochemical cycle of boron: constraints from boron isotope partitioning experiments between mica and fluid. *Lithos* **84**, 206–216.

Wunder B., Meixner A., Romer R. L. and Heinrich W. (2006) Temperature-dependent isotopic fractionation of lithium between clinopyroxene and high-pressure hydrous fluids. *Contrib. Mineral. Petrol.* **151**, 112–120.

Zack T., Foley S. F. and Rivers T. (2002) Equilibrium and disequilibrium trace element partitioning in hydrous eclogites (Trescolmen, Central Alps). *J. Petrol.* **43**, 1947–1974.

Zanetti A., D'Antonio M., Spadea P., Raffone N. and Vannucci R. (2006) Petrogenesis of mantle peridotites from the Izu–Bonin–Mariana (IBM) Forearc. *Ofioliti* **31**, 189–206.